AIMS Mathematics, 11(2): 3594–3635.
DOI:10.3934/math.2026147
Received: 28 September 2025
Revised: 06 January 2026
Accepted: 22 January 2026
Published: 06 February 2026

https://www.aimspress.com/journal/Math

Research article

A nonconvex total variational model for the joint image segmentation and restoration of images corrupted by Rician noise

Myeongmin Kang*

Department of Mathematics, Chungnam National University, Daejeon 34134, Korea

* **Correspondence:** Email: myeongminkang@cnu.ac.kr; Tel: +820428216532.

Abstract: In this paper, a novel variational model is proposed for image segmentation via joint restoration of images corrupted by blurring and Rician noise. The proposed model is built upon the piecewise constant Mumford–Shah framework and combines an appropriate data fidelity term with nonconvex total variation (NTV) regularization. The NTV regularization effectively denoises homogeneous regions while accurately preserving object boundaries to facilitate robust segmentation. To solve the resulting nonconvex optimization problem, a proximal alternating minimization algorithm is employed. In addition, an iteratively reweighted ℓ_1 algorithm and the alternating direction method of multipliers are adopted to efficiently handle the corresponding subproblems. Numerical experiments demonstrate the effectiveness of the proposed model in achieving accurate and robust segmentation performance when compared with several state-of-the-art methods.

Keywords: image segmentation; image restoration; Rician noise; nonconvex total variation; proximal alternating minimization algorithm
Mathematics Subject Classification: 65K10, 68U10, 94A08

1. Introduction

Image segmentation is a key topic in image processing. The aim of image segmentation is to divide an image domain into multiple segments such that each segment represents a meaningful object. Over the past few decades, numerous numerical algorithms for image segmentation have been studied, including thresholding-based algorithms [1,2], clustering methods [3–5], and graph-based methods [6–8]. Variational level set approaches have been widely applied to image segmentation and have yielded promising results.

The Mumford–Shah model [9] is one of the most well-known variational approaches and approximates an image by a piecewise-smooth function. Chan et al. [10] proposed a piecewise-constant active contour model for image segmentation, which is often referred to as the Chan–Vese

(CV) model. Lee et al. [11] extended the CV model by adopting two shifted Heaviside functions. A common drawback of these models is that they tend to yield unsatisfactory performance when segmenting images corrupted by blur and noise. Cai et al. [12] proposed a two-phase segmentation model that elucidates the relationship between image segmentation and restoration. Bar et al. [13] integrated the Mumford–Shah model with blind deconvolution of isotropic Gaussian blur. More recently, Cai et al. [14] proposed a variational model for multiphase image segmentation that combines a data fidelity term for image restoration with a variational segmentation framework.

Over the past few decades, magnetic resonance imaging (MRI) techniques have been extensively applied in medical imaging. However, noise is inevitably introduced during the image acquisition process, which degrades the image quality. Noise arises in the measured magnitude image because the real and imaginary components are corrupted. Because these components are affected by zero-mean, uncorrelated Gaussian noise with identical variance, the measured magnitude MR image is commonly modeled by a Rician distribution.

Many filtering-based approaches have been proposed for Rician noise removal, including anisotropic diffusion filters [15, 16], wavelet-based filters [17, 18], and nonlocal means filters [19, 20]. To restore images corrupted by blur and Rician noise, several variational models have also been developed. Basu et al. [21] derived a log-likelihood term based on the Rician distribution. Building on this work, Getreuer et al. [22] proposed a total variation-based model for Rician noise removal and deblurring; however, this model is nonconvex due to the data fidelity term, and a convex approximation was also suggested in [22], which is computationally complex. Chen et al. [23] introduced a convex variational model by adding a quadratic penalty term to ensure convexity of the data fidelity function. Martin et al. [24] provided a mathematical analysis demonstrating the effectiveness of nonconvex data fidelity terms for Rician denoising and proposed an efficient algorithm to solve the resulting nonconvex minimization problem. More recently, Phan et al. [25] introduced a spatially variant high-order variational model that adjusts the local regularization strength to reduce staircase artifacts while preserving edges. Brzostowski et al. [26] proposed a two-step MRI denoising method combining 2D variational mode decomposition with fused lasso to effectively suppress Rician noise. Convergent plug-and-play frameworks [27] have also been proposed.

On the other hand, MR image segmentation is a fundamental problem in medical image processing. The quality of MR image segmentation is strongly affected by Rician noise and blur. Despite the importance of this problem, relatively limited research has been devoted to segmenting images contaminated by Rician noise. Wu et al. [28] proposed a method for brain MR image segmentation by fitting a Rician probability density function. More recently, Chen et al. [29] proposed a two-step variational framework for segmenting images corrupted by Rician noise and blur, inspired by two-stage methods developed for Poisson noise.

In addition to variational approaches, deep learning approaches have been applied to MRI under Rician noise. For MR denoising, a residual convolutional network (CNN) [30], a RicianNet with a progressive network learning strategy [31], and a wider CNN [32] have been proposed to remove Rician noise effectively. For MR segmentation, deep learning models such as TransUNet, SwinUNet, and U-Net have been evaluated for robustness to Rician noise in cardiac MR images [33]. These learning-based approaches complement the theoretical strengths of variational frameworks and provide a modern benchmark for empirical performance.

In variational models, the objective function typically consists of a data fidelity term and a

regularization term. Total variation (TV) [34] is a well-known regularizer with edge-preserving properties. Previous studies [35, 36] have shown that nonconvex regularizers can outperform convex ones in certain scenarios. For example, Krishnan and Fergus [37] proposed a nonconvex TV-based model motivated by the observation that natural image gradients exhibit heavy-tailed distributions. Various other nonconvex TV regularizers have also been proposed [38], including logarithmic, fractional, and L_q-norm-based formulations.

Nonconvex optimization arises in numerous applications, including image processing, signal recovery, and machine learning. The proximal alternating minimization algorithm (PAMA) [39] established a theoretical foundation by proving the convergence of solutions to nonconvex problems involving coupled functions with two variables. Subsequent to this finding, a general convergence framework [40] was developed for descent methods applied to functions satisfying the Kurdyka–Łojasiewicz inequality. Ochs et al. [41] introduced an iterative convex majorization–minimization algorithm to solve nonsmooth, nonconvex minimization problems. Various extensions of the alternating direction method of multipliers (ADMM) have been developed to solve linearly constrained nonconvex problems. These extensions include ADMM for nonconvex problems involving difference-of-convex functions [42], linearized ADMM for image restoration with nonconvex regularization [43], and inertial ADMM for image deblurring [44].

In this work, the author proposes a novel variational model for segmenting images corrupted by Rician noise and blur, formulated through a coupled restoration–segmentation framework. Inspired by [14], the model involves two data fidelity terms associated with a latent restoration variable and the segmentation function, respectively. In contrast to existing approaches, the author incorporates a double-regularization strategy, in which nonconvex total variation (NTV) is employed to promote piecewise smoothness and preserve sharp boundaries while suppressing noise in the coupled formulation. To solve the resulting nonconvex and nonsmooth optimization problem, a proximal alternating minimization algorithm and an iteratively reweighted strategy are employed. Subproblems are efficiently solved using the alternating direction method of multipliers, leading to an effective numerical algorithm.

The main contributions of this work are summarized as follows:

- The author extends existing single-regularization models [14] to address the segmentation of images corrupted by Rician noise and blur by introducing a coupled formulation with double regularization.
- It is shown that the two regularization terms act complementarily in controlling noise suppression and geometric regularity within the segmentation process.
- A PAMA-based algorithm with three subproblems is developed, and a rigorous convergence analysis is established, extending existing PAMA results that involve two subproblems.

The outline of the remainder of this paper is as follows. Section 2 reviews existing variational models for image segmentation. Section 3 introduces the proposed variational model for image segmentation based on a coupled restoration–segmentation formulation. In Section 4, we present the numerical algorithm for solving the proposed model. In Section 5, numerical experiments are presented to demonstrate the effectiveness of the proposed method and to compare it with several state-of-the-art models. Finally, Section 6 concludes the paper.

2. Related image segmentation models

Let Ω be an open bounded domain in $\mathbb{R}^2$, and let $E \subseteq \Omega$ denote the edge set of Ω. In a variational framework for image segmentation, the Mumford–Shah model [9] is a fundamental approach and serves as the basis for many segmentation models:

$$\min_{u,S} \frac{\mu}{2} \int_{\Omega \setminus S} (u - f)^2 \, dx + \frac{\lambda}{2} \int_{\Omega \setminus S} |\nabla u|^2 \, dx + \int_S d\mathcal{H},$$

where λ and μ are positive parameters. The resulting image u approximates the given image f by a piecewise-smooth function, and the edge set S represents the segmentation boundaries. However, the original Mumford–Shah model tends to be computationally expensive.

For piecewise-constant segmentation, a simplified variant of the Mumford–Shah model was proposed:

$$\min_{u,S} \frac{\mu}{2} \int_{\Omega \setminus S} (u - f)^2 \, dx + \int_S d\mathcal{H},$$

where u is constant on each connected component of $\Omega \setminus S$.

Based on the Mumford–Shah model, the multiphase CV model [45] was introduced using multiple level set functions to represent multiple regions:

$$\begin{aligned} \min_{u,S} \quad & \frac{\mu}{2} \sum_{i=1}^{K} \int_\Omega (f - c_i)^2 u_i \, dx + \sum_{j=1}^{M} \int_\Omega |\nabla v_j| \, dx, \\ \text{s.t.} \quad & \sum_{i=1}^{K} u_i = 1, \quad u_i \in \{0, 1\}, \end{aligned}$$

where $K = 2^M$ and each u_i represents a region determined by the level set functions v_j. For $M = 2$, u_i can be expressed as

$$u_1 = v_1 v_2, \quad u_2 = v_1(1 - v_2), \quad u_3 = (1 - v_1)v_2, \quad u_4 = (1 - v_1)(1 - v_2).$$

Because the CV model is nonconvex, it is difficult to solve directly. As a result, convex relaxation techniques for image segmentation have been developed. A convex relaxation of the CV model was proposed in [46]:

$$\begin{aligned} \min_{u,S} \quad & \frac{\mu}{2} \sum_{i=1}^{K} \int_\Omega (f - c_i)^2 u_i \, dx + \sum_{j=1}^{M} \int_\Omega |\nabla v_j| \, dx, \\ \text{s.t.} \quad & \sum_{i=1}^{K} u_i = 1, \quad u_i \in [0, 1]. \end{aligned}$$

The TV fuzzy c-means (TVFBS) method [47] was also proposed:

$$\min_{u,S} \quad \frac{\mu}{2} \sum_{i=1}^{K} \int_\Omega (f - c_i)^2 u_i \, dx + \sum_{i=1}^{K} \int_\Omega |\nabla u_i| \, dx,$$

$$\text{s.t.} \quad \sum_{i=1}^{K} u_i = 1, \quad u_i \geq 0.$$

For fixed c_i, $i = 1, \ldots, K$, this formulation is closely related to the convex TV denoising model [34]. The CV and TVFBS models have demonstrated effectiveness in segmenting piecewise-constant images, particularly in the presence of Gaussian noise. However, they often fail to produce satisfactory results for images corrupted by other types of noise or blur.

To address images degraded by Gaussian noise and blur, a two-step algorithm was proposed in [12]. In the first step, the following convex image restoration problem is solved:

$$\min_u \frac{\mu}{2} \int_\Omega (f - Au)^2 \, dx + \frac{\lambda}{2} \int_\Omega |\nabla u|^2 \, dx + \int_\Omega |\nabla u| \, dx.$$

In the second step, segmentation is performed by thresholding the restored image using a clustering method. This approach was extended in [29, 48] to handle images corrupted by other types of noise, such as Poisson and Rician noise.

More recently, Cai et al. [14] proposed a variational segmentation model coupled with image restoration:

$$\begin{aligned} \min_{u_i, g} \quad & \mu\Phi(f, Ag) + \lambda \sum_{i=1}^{K} \Psi(g, u_i, c_i) + \sum_{i=1}^{K} \int_\Omega |\nabla u_i| \, dx, \\ \text{s.t.} \quad & \sum_{i=1}^{K} u_i = 1, \quad u_i \in \{0, 1\}, \end{aligned}$$

where Φ denotes the data fidelity term for image restoration and Ψ represents the data fidelity term for image segmentation. This model was shown to produce satisfactory segmentation results for images corrupted by blur and noise. Unlike existing approaches that employ TV regularization on u_i, our proposed model introduces a double NTV regularization strategy. This double regularization decouples noise suppression from geometric regularity, which cannot be achieved using a single regularization term. Further details are presented in the next section.

3. Proposed model

First we recall the coupled variational framework proposed in [14] with setting $\Psi(g, u_i, c_i) := \int_\Omega (g - c_i)^2 u_i dx$:

$$\begin{aligned} \min_{u_i, g} \quad & \mu\Phi(f, Ag) + \lambda \sum_{i=1}^{K} \int_\Omega (g - c_i)^2 u_i \, dx + \sum_{i=1}^{K} \int_\Omega |\nabla u_i| \, dx, \\ \text{s.t.} \quad & \sum_{i=1}^{K} u_i = 1, u_i \in \{0, 1\}, \end{aligned}$$

where A is a linear blurring operator, and Φ is a data fidelity term that can be changed depending upon the noise distribution. The data fidelity term, denoted by the symbol Φ, serves to approximate the variable g to the observed image f. However, this model does not include a regularization term

for g and instead imposes regularization only on the boundaries of the segmented regions through the variables u_i. Consequently, the smoothness of g is enforced only implicitly via the coupling term $\int_\Omega (g-c_i)^2 u_i \, dx$, which may result in insufficient denoising. This limitation is particularly evident when the observed image is corrupted by blur and Rician noise, as the reconstruction of g becomes highly sensitive to noise. In contrast, a model with regularization only on g would not directly control the geometric complexity of the segmentation because the regularity of region boundaries is primarily determined by the regularization of u_i. These observations suggest that a balanced treatment of both g and u_i is necessary. From a modeling perspective, g represents the latent clean image, and u_i encodes the segmentation of homogeneous regions. Each variable requires dedicated regularization to fulfill its respective role. This consideration naturally motivates the introduction of regularization terms on both g and u_i, yielding a formulation that enhances segmentation accuracy while simultaneously stabilizing the restoration of the underlying image. The author proposes a new variational model with double regularization terms for joint segmentation and restoration of a single image polluted by Rician noise and blur. The specific description of our model is as follows:

$$\begin{aligned} \min_{u_i,g} \quad & \mu \int_\Omega G(Ag)\, dx + \gamma \int_\Omega \log(1+\rho|\nabla g|)\, dx + \lambda \sum_{i=1}^{K} \int_\Omega (g-c_i)^2 u_i \, dx \\ & + \sum_{i=1}^{K} \int_\Omega \log(1+\rho|\nabla u_i|)\, dx \\ \text{s.t.} \quad & \sum_{i=1}^{K} u_i = 1, 0 \le u_i \le 1, \end{aligned} \tag{3.1}$$

where the data fidelity function G is defined as

$$G(Ag) = \frac{1}{2\sigma^2}(Ag)^2 - \log I_0\Big(\frac{f(Ag)}{\sigma^2}\Big) + \frac{1}{\sigma}(\sqrt{Ag} - \sqrt{f})^2,$$

and I_0 denotes the modified Bessel function of order zero. From a Rician distribution and maximum a posteriori estimation, the function $\frac{1}{2\sigma^2}(Au)^2 - \log I_0\Big(\frac{f(Au)}{\sigma^2}\Big)$ can be derived as a data fidelity function. However, this function is nonconvex. Chen et al. [23] suggested a convex data fidelity function G, which they obtained by inserting a penalty term. Specifically, it is shown in [23, Remark 1] that the data fidelity function $G(Au)$ is strictly convex when $\sigma > 4.5$. The function $|\nabla u_i|$ or $|\nabla g|$ represents the isotropic total variation, defined as

$$|\nabla u| = \sqrt{|\nabla_x u|^2 + |\nabla_y u|^2}.$$

Our model utilizes a nonconvex log function for the NTV. It is important to note that the nonconvex log functional is similar to the ℓ_1-norm, where $|\nabla u| = 0$. However, this is smaller than the ℓ_1 norm as $|\nabla u|$ approaches ∞. This observation shows that the nonconvex log functional enables homogeneous regions to be well-smoothed with the edges and details preserved. Here, ρ is a positive parameter that controls the nonconvexity of two regularizing terms.

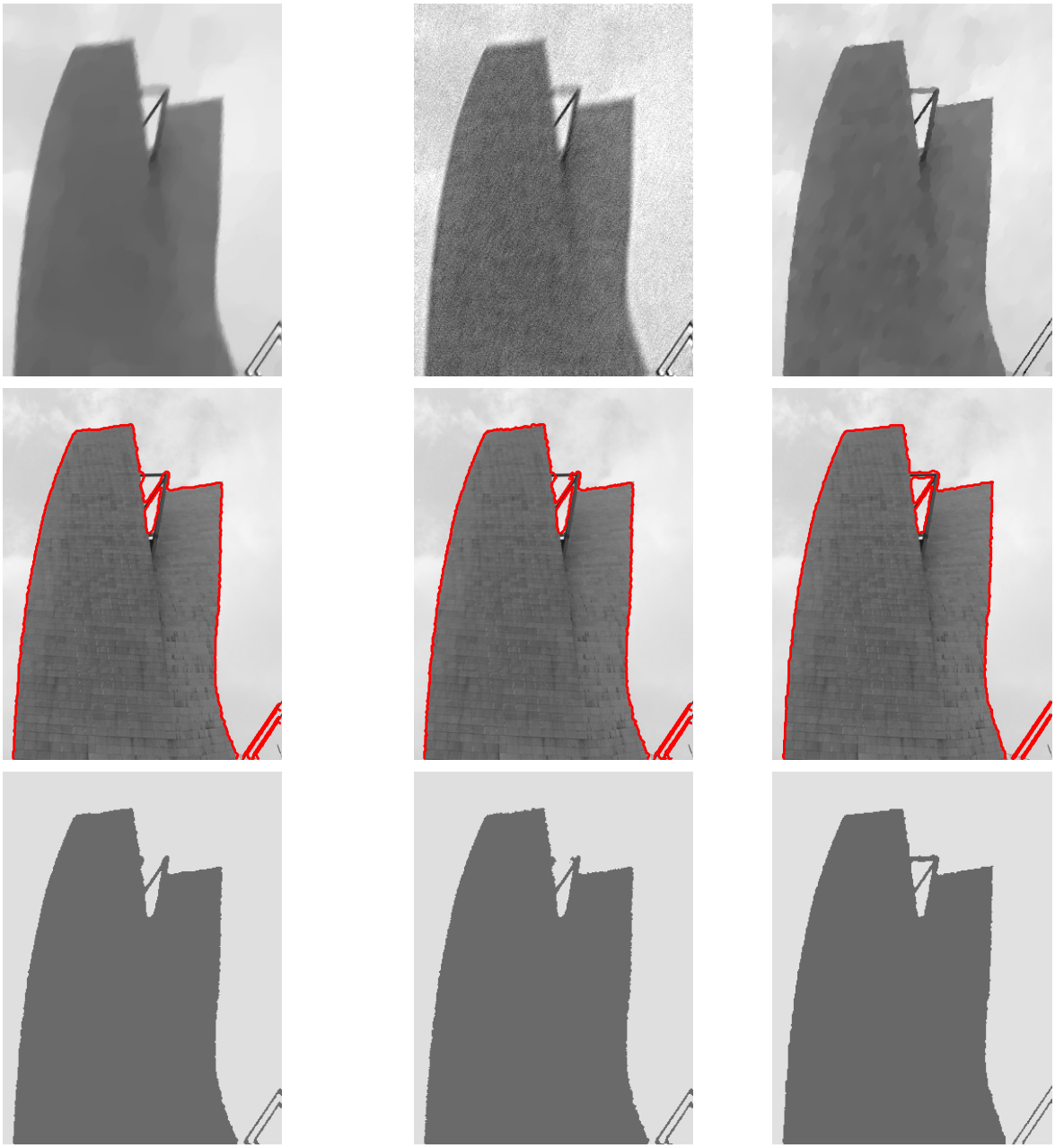

(a) our model without NTV for u_i (b) our model without NTV for g (c) our model

Figure 1. Comparison of reconstruction and segmentation results under different regularization strategies. Columns (a)–(c) correspond to: (a) the proposed model without NTV regularization on u_i, (b) the proposed model without NTV regularization on g, and (c) the proposed model with double regularization. Rows from top to bottom show restoration results of g, segmentation results, and the corresponding approximated images. The quantitative performance in terms of (Accuracy, F-measure) is (a) (0.9851, 0.9849), (b) (0.9846, 0.9844), and (c) (0.9864, 0.9862).

We adopt the convex relaxation $u \in [0, 1]$ for constraint $u \in \{0, 1\}$.

The proposed model (3.1) employs double regularization on both g and u_i. To investigate the

effect of double regularization on segmentation performance, the model is compared with two single-regularization variants, where regularization is applied only to g or only to u_i. The corresponding results are shown in Figure 1.

When regularization is applied only to g, explicit length control of the segmented curves is not available. Consequently, to suppress noise and stabilize the segmentation, the regularization on g must be relatively large. This results in oversmoothing of the reconstructed image g, causing thin structural regions between adjacent buildings to be blurred. Because the segmentation relies on the intensity information of g, the loss of these fine structures directly degrades segmentation performance. Although the main building boundaries are still reasonably captured, thin structures are not accurately recovered.

When regularization is applied only to u_i, no regularization is imposed on g. As a result, the reconstruction of g remains noisy and slightly blurry, which negatively affects the segmentation process. The segmented boundaries are consequently less smooth, and fine structures are not accurately reconstructed.

When double regularization is employed, the reconstruction of g achieves a proper balance between denoising and deblurring, and the lengths of the segmented boundaries are effectively controlled. As a result, both the main building boundaries and thin structural regions are segmented more accurately. These observations clearly demonstrate the necessity and effectiveness of incorporating double regularization in the proposed model.

4. Proposed algorithm

4.1. Proximal alternating minimization algorithm

To apply a numerical algorithm, we first discretize the proposed model (3.1) as follows:

$$\begin{aligned} \min_{g,c_i,u_i} \quad & \mu \sum_{\Omega} G(Ag) + \gamma \sum_{j\in\Omega} \log(1+\rho|\nabla g|) + \lambda \sum_{i=1}^{K} \sum_{\Omega} (g-c_i)^2 u_i + \sum_{i=1}^{K} \sum_{\Omega} \log(1+\rho|\nabla u_i|) \\ \text{s.t.} \quad & \sum_{i=1}^{K} u_i = 1,\ 0 \le u_i \le 1,\ 0 \le Ag \le 255,\ 0 \le c_i \le 255. \end{aligned}$$

Let $S := \{y \in \Omega \times \mathbb{R}^K : \sum_{i=1}^{K} y_i = 1, y \ge 0\}$, $S_1 = \{y \in \Omega : 0 \le y \le 255\}$ and $S_2 = \{y \in \mathbb{R}^K : 0 \le y_i \le 255\}$. The proposed model (4.1) can be equivalent to the following unconstrained minimization problem:

$$\begin{aligned} \min_{g,c_i,u_i} \quad & \mu \sum_{\Omega} G(Ag) + \gamma \sum_{j\in\Omega} \log(1+\rho|\nabla g|) + \lambda \sum_{i=1}^{K} \sum_{\Omega} (g-c_i)^2 u_i \\ & + \sum_{i=1}^{K} \sum_{\Omega} \log(1+\rho|\nabla u_i|) + \mathcal{I}_S(u_1, u_2, \cdots, u_K) + \mathcal{I}_{S_1}(Ag) + \mathcal{I}_{S_2}(c_1, \cdots, c_K), \end{aligned} \tag{4.1}$$

where $\mathcal{I}_S$, $\mathcal{I}_{S_1}$, and $\mathcal{I}_{S_2}$ are the indicator functions of S, S_1, and S_2, respectively. The indicator function of a set B is defined as

$$\mathcal{I}_B(y) = \begin{cases} 0, & y \in B, \\ \infty, & \text{otherwise.} \end{cases}$$

Bacause the discretized model (4.1) has multiple variables and involves the coupled term $\lambda \sum_{i=1}^{K} \sum_{\Omega}(g-c_i)^2 u_i$, it is difficult to solve this model directly. Existing ADMM [42–44] and PAMA [39] algorithms are primarily designed for two-variable optimization problems, and their direct extension to a three-variable setting is not theoretically justified. To address this limitation, the author extends PAMA to handle multiple coupled variables, providing a flexible and convergent framework suitable for the proposed model. In this extended PAMA, the objective function is alternately minimized with a proximal term for one variable while keeping the others fixed.

For the proposed model, the PAMA consists of the following iterative steps:

$$\begin{cases} g^{k+1} &= \arg\min\limits_{g} \ \mu \sum\limits_{\Omega} G(Ag) + \gamma \sum\limits_{j\in\Omega} \log(1+\rho|\nabla g|) + \lambda \sum\limits_{i=1}^{K} \sum\limits_{\Omega} (g-c_i^k)^2 u_i^k + \mathcal{I}_{S_1}(Ag) \\ & \qquad + \dfrac{\delta}{2}\|g-g^k\|_2^2, \\ c_i^{k+1} &= \arg\min\limits_{c_i} \lambda \sum\limits_{\Omega} (g^{k+1}-c_i)^2 u_i^k + \mathcal{I}_{S_2}(c_1,\cdots,c_K) + \dfrac{\delta}{2}\|c_i - c_i^k\|_2^2, \quad i=1,\cdots,K, \\ \begin{pmatrix} u_1^{k+1} \\ u_2^{k+1} \\ \vdots \\ u_K^{k+1} \end{pmatrix} &= \arg\min\limits_{u_i} \lambda \sum\limits_{i=1}^{K} \sum\limits_{\Omega} (g^{k+1}-c_i^{k+1})^2 u_i + \sum\limits_{i=1}^{K} \sum\limits_{\Omega} \log(1+\rho|\nabla u_i|) + \mathcal{I}_S(u_1,\cdots,u_K) \\ & \qquad + \dfrac{\delta}{2} \sum\limits_{i=1}^{K} \|u_i - u_i^k\|_2^2. \end{cases} \tag{4.2}$$

Let F be the objective function of the problem (4.1):

$$\begin{aligned} F(g,c_i,u_i;i=1,\cdots,K) \ := \ & \mu \sum_{\Omega} G(Ag) + \gamma \sum_{\Omega} \log(1+\rho|\nabla g|) + \mathcal{I}_{S_1}(Ag) \\ & + \lambda \sum_{i=1}^{K} \sum_{\Omega} (g-c_i)^2 u_i + \sum_{i=1}^{K} \sum_{\Omega} \log(1+\rho|\nabla u_i|) \\ & + \mathcal{I}_{S_2}(c_1,\cdots,c_K) + \mathcal{I}_S(u_1,u_2,\cdots,u_K). \end{aligned}$$

For simple notation, we set

$$\begin{aligned} F_1(g) &= \mu \sum_{\Omega} G(Ag) + \gamma \sum_{\Omega} \log(1+\rho|\nabla g|) + \mathcal{I}_{S_1}(Ag), \\ F_2(u_1,u_2,\cdots,u_K) &= \sum_{i=1}^{K} \sum_{\Omega} \log(1+\rho|\nabla u_i|) + \mathcal{I}_S(u_1,u_2,\cdots,u_K), \\ F_3(c_1,c_2,\cdots,c_K) &= \mathcal{I}_{S_2}(c_1,c_2,\cdots,c_K), \\ H(g,c_i,u_i;i=1,\cdots,K) &= \lambda \sum_{i=1}^{K} \sum_{\Omega} (g-c_i)^2 u_i. \end{aligned}$$

Then, $F(g,c_i,u_i) = F_1(g) + F_2(u_1,\cdots,u_K) + F_3(c_1,c_2,\cdots,c_K) + H(g,c_i,u_i)$.

In order to demonstrate the convergence of the PAMA (4.2), it is first necessary to establish the boundedness of a subgradient of F at $(g^{k+1}, c_i^{k+1}, u_i^{k+1})$.

Lemma 4.1. *Let the sequence* $\{\mathbf{X}^k\} = \{(g^k, c_i^k, u_i^k) : i = 1, \cdots, K\}$ *be generated by the PAMA (4.2). There exist a sequence* $\{\boldsymbol{P}^{k+1}\} = \{(p_g^{k+1}, p_i^{k+1}, q_i^{k+1}) : i = 1, \cdots, K\} \in \partial F(\boldsymbol{X}^{k+1})$ *and a constant* β *such that*

$$\|\boldsymbol{P}^{k+1}\|_2 \leq \beta \|\boldsymbol{X}^{k+1} - \boldsymbol{X}^k\|_2. \tag{4.3}$$

Proof. The PAMA can be rewritten as follows:

$$g^{k+1} = \arg\min_g \; F(g, c_i^k, u_i^k) + \frac{\delta}{2}\|g - g^k\|_2^2, \tag{4.4}$$

$$\begin{pmatrix} c_1^{k+1} \\ c_2^{k+1} \\ \vdots \\ c_K^{k+1} \end{pmatrix} = \arg\min_{c_i} \; F(g^{k+1}, c_i, u_i^k) + \frac{\delta}{2}\sum_{i=1}^{K}\|c_i - c_i^k\|_2^2, \tag{4.5}$$

$$\begin{pmatrix} u_1^{k+1} \\ u_2^{k+1} \\ \vdots \\ u_K^{k+1} \end{pmatrix} = \arg\min_{u_i} \; F(g^{k+1}, c_i^{k+1}, u_i) + \frac{\delta}{2}\sum_{i=1}^{K}\|u_i - u_i^k\|_2^2. \tag{4.6}$$

By optimality conditions of the subproblems (4.4)–(4.6), we have

$$\begin{aligned}
0 &\in \partial_g F(g^{k+1}, c_i^k, u_i^k) + \delta(g^{k+1} - g^k) \\
&= \partial_g F_1(g^{k+1}) + \nabla_g H(g^{k+1}, c_i^k, u_i^k) + \delta(g^{k+1} - g^k), \\
0 &\in \partial_{c_j} F(g^{k+1}, c_i^{k+1}, u_i^k) + \delta(c_j^{k+1} - c_j^k) \\
&= \partial_{c_j} F_3(c_i^{k+1}) + \nabla_{c_j} H(g^{k+1}, c_i^{k+1}, u_i^k) + \delta(c_j^{k+1} - c_j^k), \quad j = 1, \cdots, K, \\
0 &\in \partial_{u_j} F(g^{k+1}, c_i^{k+1}, u_i^{k+1}) + \delta(u_j^{k+1} - u_j^k) \\
&= \partial_{u_j} F_2(u_i^{k+1}) + \nabla_{u_j} H(g^{k+1}, c_i^{k+1}, u_i^{k+1}) + \delta(u_j^{k+1} - u_j^k), \quad j = 1, \cdots, K.
\end{aligned}$$

Hence, a subgradient of F at $(g^{k+1}, c_i^{k+1}, u_i^{k+1})$ can be obtained:

$$\begin{aligned}
p_g^{k+1} &:= -\delta(g^{k+1} - g^k) - \nabla_g H(g^{k+1}, c_i^k, u_i^k) + \nabla_g H(g^{k+1}, c_i^{k+1}, u_i^{k+1}) \\
&\in \partial_g F(g^{k+1}, c_i^{k+1}, u_i^{k+1}) \\
p_j^{k+1} &:= -\delta(c_j^{k+1} - c_j^k) - \nabla_{c_j} H(g^{k+1}, c_i^{k+1}, u_i^k) + \nabla_{c_j} H(g^{k+1}, c_i^{k+1}, u_i^{k+1}) \\
&\in \partial_{c_j} F(g^{k+1}, c_i^{k+1}, u_i^{k+1}), \quad j = 1, \cdots, K. \\
q_j^{k+1} &:= -\delta(u_j^{k+1} - u_j^k) \\
&\in \partial_{u_j} F(g^{k+1}, c_i^{k+1}, u_i^{k+1}), \quad j = 1, \cdots, K.
\end{aligned}$$

Because $Ag \in [0, 255]$ and A is a bounded linear operator, g is also bounded, so there exists $M > 0$ s.t. $|g| \leq M$. By using the boundedness of $g, c_j \in [0, 255], u_j \in [0, 1]$ and

$$\nabla_g H(g, c_i, u_i) = 2\lambda \sum_{i=1}^{K}(g - c_i)u_i,$$

The following inequalities can be obtained:

$$\begin{aligned}
&\|\nabla_g H(g^{k+1}, c_i^k, u_i^k) - \nabla_g H(g^{k+1}, c_i^{k+1}, u_i^{k+1})\|_2 \\
&\qquad = \left\| 2\lambda \sum_{i=1}^{K} ((g^{k+1} - c_i^k)u_i^k - (g^{k+1} - c_i^{k+1})u_i^{k+1}) \right\|_2 \\
&\qquad \le 2\lambda \sum_{i=1}^{K} \|g^{k+1}(u_i^k - u_i^{k+1})\|_2 + 2\lambda \sum_{i=1}^{K} \|c_i^k u_i^k - c_i^{k+1} u_i^{k+1}\|_2 \\
&\qquad \le 2 \cdot M\lambda \sum_{i=1}^{K} \|u_i^k - u_i^{k+1}\|_2 + 2\lambda \sum_{i=1}^{K} \sqrt{255^2 + 1^2}(|c_i^k - c_i^{k+1}| + \|u_i^k - u_i^{k+1}\|_2),
\end{aligned}$$

where third inequality can be obtained by the Lipschitz continuity of the bilinear mapping $\phi(c, u) = cu$ on the compact set $[0, 255] \times [0, 1]$ with Lipschitz constant $\sqrt{255^2 + 1^2}$ for each coordinate function $c_i \cdot u_i(i_x, i_y)$ at $(i_x, i_y) \in \Omega$. Similarly, the following inequalities are obtained:

$$\begin{aligned}
&|\nabla_{c_j} H(g^{k+1}, c_i^{k+1}, u_i^k) - \nabla_{c_j} H(g^{k+1}, c_i^{k+1}, u_i^{k+1})| \\
&\qquad = \left| 2\lambda \sum_{\Omega} (c_j^{k+1} - g^{k+1})u_j^k - 2\lambda \sum_{\Omega} (c_j^{k+1} - g^{k+1})u_j^{k+1} \right| \\
&\qquad = \left| 2\lambda \sum_{\Omega} (c_j^{k+1} - g^{k+1})(u_j^k - u_j^{k+1}) \right| \\
&\qquad \le 2 \cdot (255 + M)\lambda \sum_{\Omega} |u_j^k - u_j^{k+1}| \\
&\qquad \le 2 \cdot (255 + M)\lambda \sqrt{|\Omega|} \|u_j^k - u_j^{k+1}\|_2,
\end{aligned}$$

where the last inequality can be obtained from the inequality

$$\|x\|_1 \le \sqrt{d}\|x\|_2, \quad \forall x \in \mathbb{R}^d.$$

Thus,

$$\left\| \begin{pmatrix} p_g^{k+1} \\ p_1^{k+1} \\ \vdots \\ p_K^{k+1} \\ q_1^{k+1} \\ \vdots \\ q_K^{k+1} \end{pmatrix} \right\|_2 \le \delta\|g^{k+1} - g^k\|_2 + (L_1 + \delta) \sum_{i=1}^{K} |c_i^k - c_i^{k+1}| + (L_2 + \delta) \sum_{i=1}^{K} \|u_i^k - u_i^{k+1}\|_2,$$

where $L_1 = 2\lambda \sqrt{255^2 + 1^2}$, $L_2 = L_1 + 2 \cdot M\lambda + 2 \cdot (255\lambda + M\lambda) \sqrt{|\Omega|}$. □

For the convergence of PAMA, the following two assumptions are imposed:

A1 $f \in L^\infty(\Omega)$ with $\inf_\Omega f > 0$ and $\sigma > 4.5$.

A2 $Ag^0 \in S_1$, $(c_i^0; i = 1, \ldots, K) \in S_2$, and $(u_i^0; i = 1, \ldots, K) \in S$.

Under assumption A1, it follows from [23, Theorem 1] that G is strictly convex and bounded from below. Assumption A2 ensures that the sequence of objective function values generated by PAMA remains bounded. Together, these properties provide the foundation for the convergence analysis of PAMA. Based on these assumptions, the convergence of PAMA is established in the following theorem.

Theorem 4.1. *Let f be in $L^\infty(\Omega)$ with $\inf_\Omega f > 0$. Assume that $\sigma > 4.5$, and the initial value $\mathbf{X}^0 = (g^0, c_i^0, u_i^0; i = 1, \cdots, K)$ of the PAMA (4.2) is selected by satisfying $Ag^0 \in S_1$, $(c_i^0; i = 1, \cdots, K) \in S_2$, and $(u_i^0; i = 1, \cdots, K) \in S$. The PAMA (4.2) returns a stationary point of the problem (4.1) or, in the event that it generates an infinite sequence, the following conditions must hold:*
For the sequence $\{\mathbf{X}^k\} = \{(g^k, c_i^k, u_i^k) : i = 1, \cdots, K\}$ generated by the PAMA (4.2),

(A) $\{F(\mathbf{X}^k)\}$ is monotonically decreasing and convergent to some F^*.

(B) $\sum_{k=1}^{\infty} \|\mathbf{X}^{k+1} - \mathbf{X}^k\|_2^2 < +\infty$ is satisfied. Hence, $\lim_{k\to\infty} \|\mathbf{X}^{k+1} - \mathbf{X}^k\| = 0$.

(C) There exists a subsequence $\{\mathbf{X}^{k_\ell}\}$ of $\{\mathbf{X}^k\}$ converging to a limit point $\bar{\mathbf{X}} = (\bar{g}, \bar{c}_i, \bar{u}_i; i = 1, \cdots, K)$ and $\lim_{\ell\to\infty} F(\mathbf{X}^{k_\ell}) \to F(\bar{\mathbf{X}})$. Furthermore, any limit point of $\{\mathbf{X}^k\}$ is a stationary point of (4.1).

Proof. The statements (A)–(C) of the theorem are proved.
(A) By the optimality of g^{k+1}, c_i^{k+1}, and u_i^{k+1} in (4.4)–(4.6), it follows that

$$F(g^{k+1}, c_i^k, u_i^k) + \frac{\delta}{2}\|g^{k+1} - g^k\|_2^2 \le F(g^k, c_i^k, u_i^k),$$
$$F(g^{k+1}, c_i^{k+1}, u_i^k) + \frac{\delta}{2}\sum_{i=1}^{K}\|c_i^{k+1} - c_i^k\|_2^2 \le F(g^{k+1}, c_i^k, u_i^k),$$
$$F(g^{k+1}, c_i^{k+1}, u_i^{k+1}) + \frac{\delta}{2}\sum_{i=1}^{K}\|u_i^{k+1} - u_i^k\|_2^2 \le F(g^{k+1}, c_i^{k+1}, u_i^k),$$

respectively. By summing the above equations, it follows that

$$F(g^{k+1}, c_i^{k+1}, u_i^{k+1}) + \frac{\delta}{2}\|g^{k+1} - g^k\|_2^2 + \frac{\delta}{2}\sum_{i=1}^{K}\|c_i^{k+1} - c_i^k\|_2^2 + \frac{\delta}{2}\sum_{i=1}^{K}\|u_i^{k+1} - u_i^k\|_2^2 \le F(g^k, c_i^k, u_i^k). \tag{4.7}$$

This shows that $F(\mathbf{X}^k)$ is monotonically decreasing. According to [23, Theorem 1], G is bounded from below under the conditions that $f \in L^\infty(\Omega)$ with $\inf_\Omega f > 0$, and $\sigma > 4.5$. Hence, the objective function F is also bounded from below. Thus, $F(\mathbf{X}^k)$ converges.
(B) By summing from $k = 0$ to N of (4.7), it follows that

$$\frac{\delta}{2}\sum_{k=0}^{N}\|g^{k+1} - g^k\|_2^2 + \frac{\delta}{2}\sum_{i=1}^{K}\sum_{k=0}^{N}\|c_i^{k+1} - c_i^k\|_2^2 + \frac{\delta}{2}\sum_{i=1}^{K}\sum_{k=0}^{N}\|u_i^{k+1} - u_i^k\|_2^2$$

$$\leq \quad F(g^0, c_i^0, u_i^0) - F(g^{N+1}, c_i^{N+1}, u_i^{N+1}).$$

Owing to convergence of the sequence $F(g^N, C_i^N, u_i^N)$, the sequences $\{\sum_{k=0}^{N} \|g^{k+1} - g^k\|_2^2\}_N$, $\{\sum_{k=0}^{N} \|c_i^{k+1} - c_i^k\|_2^2\}_N$, and $\{\sum_{k=0}^{N} \|u_i^{k+1} - u_i^k\|_2^2\}_N$ are bounded from above. Because they are monotonically increasing sequences, the convergence follows, that is,

$$\sum_{k=1}^{\infty} \|\mathbf{X}^{k+1} - \mathbf{X}^k\|_2^2 < +\infty.$$

(C) Because $F(\mathbf{X}^0) < \infty$, and $F(\mathbf{X}^k)$ is monotonically decreasing, $F(\mathbf{X}^k)$ is bounded. Particularly, $\mathcal{I}_S(u_1^k, u_2^k, \cdots, u_K^k)$, $\mathcal{I}_{S_1}(Ag^k)$, $\mathcal{I}_{S_2}(c_1^k, \cdots, c_K^k)$ are bounded. Hence, $\{\mathbf{X}^k\}$ is bounded, and there exists a subsequence of $\{\mathbf{X}^k\}$ converging to a limit point. To establish the continuity condition, a convergent subsequence $\mathbf{X}^{k_\ell} = (g^{k_\ell}, c_i^{k_\ell}, u_i^{k_\ell})$ of $\mathbf{X}^k$ is considered such that $(g^{k_\ell}, c_i^{k_\ell}, u_i^{k_\ell}) \to (\bar{g}, \bar{c}_i, \bar{u}_i)$ as $\ell \to \infty$. $\bar{\mathbf{c}}$ and $\bar{\mathbf{u}}$ are denoted by $(\bar{c}_1, \cdots, \bar{c}_K)$ and $(\bar{u}_1, \cdots, \bar{u}_K)$, respectively. Let $p_g^{k_\ell} \in \partial F_1(g^{k_\ell})$, $p_j^{k_\ell} \in \partial_{c_j} F_3(c_i^{k_\ell})$, and $q_j^{k_\ell} \in \partial_{u_j} F_2(u_i^{k_\ell})$ be sequences satisfying

$$\begin{aligned}
\delta(g^{k_{\ell-1}} - g^{k_\ell}) &= \nabla_g H(g^{k_\ell}, c_i^{k_\ell - 1}, u_i^{k_\ell - 1}) + p_g^{k_\ell} \in \partial_g F(g^{k_\ell}, c_i^{k_\ell - 1}, u_i^{k_\ell - 1}), \\
\delta(c_j^{k_{\ell-1}} - c_j^{k_\ell}) &= \nabla_{c_j} H(g^{k_\ell}, c_i^{k_\ell}, u_i^{k_\ell - 1}) + p_j^{k_\ell} \in \partial_{c_j} F(g^{k_\ell}, c_i^{k_\ell}, u_i^{k_\ell - 1}), \quad j = 1, \ldots, K, \\
\delta(u_j^{k_{\ell-1}} - u_j^{k_\ell}) &= \nabla_{u_j} H(g^{k_\ell}, c_i^{k_\ell}, u_i^{k_\ell}) + q_j^{k_\ell} \in \partial_{u_j} F(g^{k_\ell}, c_i^{k_\ell}, u_i^{k_\ell}), \quad j = 1, \ldots, K.
\end{aligned}$$

Because the sequences $(g^{k_\ell}, c_i^{k_\ell}, u_i^{k_\ell})$ and $(g^{k_{\ell-1}}, c_i^{k_{\ell-1}}, u_i^{k_{\ell-1}})$ are contained in a compact set, the differences $\delta(g^{k_{\ell-1}} - g^{k_\ell})$, $\delta(c_j^{k_{\ell-1}} - c_j^{k_\ell})$, and $\delta(u_j^{k_{\ell-1}} - u_j^{k_\ell})$ are bounded. Moreover, since $\nabla_g H$, $\nabla_{c_j} H$, and $\nabla_{u_j} H$ are continuous for all $j = 1, \cdots, K$, it follows that $\nabla_g H(g^{k_\ell}, c_i^{k_\ell - 1}, u_i^{k_\ell - 1})$, $\nabla_{c_j} H(g^{k_\ell}, c_i^{k_\ell}, u_i^{k_\ell - 1})$, and $\nabla_{u_j} H(g^{k_\ell}, c_i^{k_\ell}, u_i^{k_\ell})$ are also bounded on this compact set. Consequently, the sequence $(p_g^{k_\ell}, p_j^{k_\ell}, q_j^{k_\ell} : j = 1, \cdots, K)$ is bounded. Let $\mathbf{p}^{k_\ell} := (p_1^{k_\ell}, \cdots, p_K^{k_\ell})$, $\mathbf{c} := (c_1, \cdots, c_K)$, $\mathbf{q}^{k_\ell} := (q_1^{k_\ell}, \cdots, q_K^{k_\ell})$, and $\mathbf{u} := (u_1, \cdots, u_K)$. Hence, $\lim_{\ell\to\infty} \langle p_g^{k_\ell}, \bar{g} - g^{k_\ell} \rangle = 0$, $\lim_{\ell\to\infty} \langle \mathbf{p}^{k_\ell}, \bar{\mathbf{c}} - \mathbf{c}^{k_\ell} \rangle = 0$, and $\lim_{\ell\to\infty} \langle \mathbf{q}^{k_\ell}, \bar{\mathbf{u}} - \mathbf{u}^{k_\ell} \rangle = 0$. By using the lower semicontinuity of F and the convexity of F_1, F_2, and F_3, it follows that

$$\begin{aligned}
F(\bar{g}, \bar{\mathbf{c}}, \bar{\mathbf{u}}) &\leq \liminf_{\ell\to\infty} F(g^{k_\ell}, \mathbf{c}^{k_\ell}, \mathbf{u}^{k_\ell}) \leq \limsup_{\ell\to\infty} F(g^{k_\ell}, \mathbf{c}^{k_\ell}, \mathbf{u}^{k_\ell}) \\
&\leq \limsup_{\ell\to\infty} H(g^{k_\ell}, \mathbf{c}^{k_\ell}, \mathbf{u}^{k_\ell}) + \limsup_{\ell\to\infty} F_1(g^{k_\ell}) + \limsup_{\ell\to\infty} F_3(\mathbf{c}^{k_\ell}) \\
&\quad + \limsup_{\ell\to\infty} F_2(\mathbf{u}^{k_\ell}) \\
&\leq H(\bar{g}, \bar{\mathbf{c}}, \bar{\mathbf{u}}) + \limsup_{\ell\to\infty} F_1(g^{k_\ell}) + \lim_{\ell\to\infty} \langle p_g^{k_\ell}, \bar{g} - g^{k_\ell} \rangle \\
&\quad + \limsup_{\ell\to\infty} F_3(\mathbf{c}^{k_\ell}) + \lim_{\ell\to\infty} \langle \mathbf{p}^{k_\ell}, \bar{\mathbf{c}} - \mathbf{c}^{k_\ell} \rangle \\
&\quad + \limsup_{\ell\to\infty} F_2(\mathbf{u}^{k_\ell}) + \lim_{\ell\to\infty} \langle \mathbf{q}^{k_\ell}, \bar{\mathbf{u}} - \mathbf{u}^{k_\ell} \rangle \\
&\leq H(\bar{g}, \bar{\mathbf{c}}, \bar{\mathbf{u}}) + \limsup_{\ell\to\infty} (F_1(g^{k_\ell}) + \langle p_g^{k_\ell}, \bar{g} - g^{k_\ell} \rangle) \\
&\quad + \limsup_{\ell\to\infty} (F_3(\mathbf{c}^{k_\ell}) + \langle \mathbf{p}^{k_\ell}, \bar{\mathbf{c}} - \mathbf{c}^{k_\ell} \rangle) \\
&\quad + \limsup_{\ell\to\infty} (F_2(\mathbf{u}^{k_\ell}) + \langle \mathbf{q}^{k_\ell}, \bar{\mathbf{u}} - \mathbf{u}^{k_\ell} \rangle)
\end{aligned}$$

$$\leq \quad H(\bar{g}, \bar{\mathbf{c}}, \bar{\mathbf{u}}) + F_1(\bar{g}) + F_3(\bar{\mathbf{c}}) + F_2(\bar{\mathbf{u}}) = F(\bar{g}, \bar{\mathbf{c}}, \bar{\mathbf{u}}).$$

Therefore, $F(g^{k_\ell}, \mathbf{c}^{k_\ell}, \mathbf{u}^{k_\ell}) \to F(\bar{g}, \bar{\mathbf{c}}, \bar{\mathbf{u}})$ as $\ell \to \infty$.

Lastly, let $\bar{\mathbf{X}}$ be a limit point of $\mathbf{X}^k$. There exists a subsequence $\{\mathbf{X}^{k_\ell}\}$ of $\{\mathbf{X}^k\}$ converging to $\bar{\mathbf{X}}$. By Lemma 4.1, there exists a sequence $\{(p_g^{k+1}, p_i^{k+1}, q_i^{k+1}) : i = 1, \cdots, K\} \in \partial F(\mathbf{X}^{k+1})$ satisfying Eq (4.3). Because the right-hand side of Eq (4.3) goes to zero as $k \to \infty$ according to (B), $\{p_g^k\}, \{p_i^k\}, \{q_i^k\}$, $i = 1, \cdots, K$ also goes to $\mathbf{0}$ as $k \to \infty$. Clearly, $\{p_g^{k_\ell}\}, \{p_i^{k_\ell}\}, \{q_i^{k_\ell}\}$, $i = 1, \cdots, K$ converge to $\mathbf{0}$. Owing to closedness [39, Remark 2.1 (b)] of ∂F and the continuity condition, $\mathbf{0} \in \partial F(\bar{\mathbf{X}})$. □

Remark 4.1. *The convergence analysis in Theorem 4.1 is limited to the boundedness of subgradients and the verification of first-order optimality conditions. Although it guarantees convergence to a critical value, it does not ensure full global convergence to a critical point. Achieving global convergence would require the objective function to satisfy the Kurdyka–Łojasiewicz (KL) inequality; however, due to the data fidelity term $G(Ag)$ associated with g, this condition is not satisfied in the proposed model. Despite this limitation, the analysis is practically sufficient, as demonstrated by numerical experiments showing stable and consistent convergence behavior across a wide range of settings.*

The c_i-subproblems have the closed form solution

$$c_i^{k+1} = \min\left(255, \max\left(0, \frac{2\lambda \sum_\Omega g^{k+1} u_i^k + \delta c_i^k}{2\lambda \sum_\Omega u_i^k + \delta}\right)\right), \quad \forall i = 1, \cdots, K.$$

The other subproblems are not solved directly, and in addition, they are nonconvex due to the NTV term. In the following subsections, the author presents iterative algorithms for solving these subproblems that utilize the iteratively reweighted ℓ_1 (IRL1) algorithm.

4.2. Iterative algorithm for the g-subproblem

First, the author recalls the IRL1 method [41] for the following nonconvex and nonsmooth optimization problem:

$$\min_v E_1(v) + E_2(E_3(v)), \tag{4.8}$$

where $E_1 : \mathbb{R}^n \to \mathbb{R} \cup \{\infty\}$ is a proper, lower semicontinuous (l.s.c.), convex function; $E_2 : \mathbb{R}^r \to \mathbb{R} \cup \{\infty\}$ is assumed to be a proper, l.s.c., concave, and coordinatewise nondecreasing function; and $E_3 : \mathbb{R}^n \to \mathbb{R}^r$ is coordinatewise convex. Furthermore, the objective function $E := E_1 + E_2(E_3)$ of (4.8) is assumed coercive and bounded from below.

Problem (4.8) is nonconvex due to E_2. The IRL1 algorithm iteratively minimizes a convex majorization of (4.8) instead of the original nonconvex function. At each iteration ℓ, the subproblem is

$$\min_v E_1(v) + \langle w^\ell, E_3(v)\rangle,$$

where w^ℓ is a limiting supergradient of E_2 at $E_3(v^\ell)$.

Applying IRL1 to the g-subproblem, we define $E_1(g) = \mu \sum_\Omega G(Ag) + \lambda \sum_{i=1}^K \sum_\Omega (g - c_i^k)^2 u_i^k + \mathcal{I}_{S_1}(Ag) + \frac{\delta}{2}\|g - g^k\|_2^2$, $E_2(v) = \gamma\langle \frac{1}{\rho}\log(1 + \rho v), \mathbf{1}\rangle$, $E_3(g) = |\nabla g|$. In this setting, all assumptions required for IRL1 are satisfied.

Applying IRL1 to the g-subproblem results in the following iterative scheme:

$$\begin{aligned} w_1^{k,\ell+1} &= \frac{1}{1+\rho|\nabla g^{k,\ell}|}, \\ g^{k,\ell+1} &= \arg\min_g \mu \sum_{\Omega} G(Ag) + \lambda \sum_{i=1}^{K} \sum_{\Omega} (g - c_i^k)^2 u_i^k + \mathcal{I}_{S_1}(Ag) + \gamma \langle w_1^{k,\ell+1}, |\nabla g| \rangle \\ &\quad + \frac{\delta}{2} \|g - g^k\|_2^2. \end{aligned} \tag{4.9}$$

The convergence of IRL1 (4.9) for solving g-subproblem can be proved.

Theorem 4.2. *It is assumed that the initial value $g^{k,0}$ of IRL1 (4.9) is chosen by satisfying $Ag^{k,0} \in S_1$. IRL1 (4.9) returns a stationary point of the g-subproblem in (4.2). Otherwise, if it generates an infinite sequence, the following conditions hold:*
For the sequence g^ℓ generated by the IRL1 (4.9),

(A) $\{E(g^{k,\ell})\}$ is monotonically decreasing and convergent to some E^*, where $E(g) := E_1(g) + E_2(E_3(g))$.

(B) $\sum_{\ell=1}^{\infty} \|g^{k,\ell+1} - g^{k,\ell}\|_2^2 < +\infty$ is satisfied. Hence, $\lim_{\ell\to\infty} \|g^{k,\ell+1} - g^{k,\ell}\| = 0$.

(C) There exists a subsequence $\{g^{k,\ell_j}\}$ of $\{g^{k,\ell}\}$ converging to a limit point $g^{k,*}$ and $\lim_{j\to\infty}\{E(g^{k,\ell})\} \to E(g^{k,*})$. Moreover, any limit point of $\{g^{k,\ell}\}$ is a stationary point of the g-subproblem in (4.2).

Proof. The significant properties of IRL1 were proved in [41, Proposition 5] under additional conditions. First, it is proved that these additional conditions hold in our setting, resulting in satisfying the properties in [41, Proposition 5].
(1) E_2 is a differentiable function, and $\nabla E_2(v) = \dfrac{\gamma}{1+\rho v}$ and $\nabla^2 E_2(v) = \operatorname{diag}(-\dfrac{\gamma\rho}{1+\rho v})$. Hence, $\|\nabla^2 E_2(v)\|_2 \le \gamma\rho$, and E_2 has Lipschitz-continuous gradients.
(2) Clearly, the convex function $v \mapsto \langle w^\ell, v\rangle$ has a globally Lipschitz-continuous gradient with a common Lipschitz constant 0.
(3) Trivially, the function $v \mapsto E_1(v) + \langle w^\ell, E_3(v)\rangle$ is strongly convex with modulus δ.
(A) From the first inequality in [41, Proposition 5], $E(g^{k,\ell})$ is monotonically decreasing. Clearly, E is bounded from below. Thus, $E(g^{k,\ell})$ converges as $\ell \to \infty$.
(B) By summing from $\ell = 0$ to N of the first inequality in [41, Proposition 5], we obtain

$$\frac{\delta}{2} \sum_{\ell=0}^{N} \|g^{k,\ell+1} - g^{k,\ell}\|_2^2 \le E(g^{k,0}) - E(g^{k,N+1}).$$

Due to convergence of the sequence $\{E(g^{k,N})\}$, the sequence $\{\sum_{\ell=0}^{N} \|g^{k,\ell+1} - g^{k,\ell}\|_2^2\}_N$ is bounded from above. Thus,

$$\sum_{\ell=1}^{\infty} \|g^{k,\ell+1} - g^{k,\ell}\|_2^2 < +\infty.$$

(C) Because $E(g^{k,\ell}) < \infty$, and $E(g^{k,\ell})$ is monotonically decreasing, $E(g^{k,\ell})$ is bounded. By the coercivity of E, $\{g^{k,\ell}\}$ is bounded, and there exists a subsequence $\{g^{k,\ell_j}\}$ converging to a limit point $g^{k,*}$. By the third

property of [41, Proposition 5], $\lim_{j\to\infty}\{E(g^{k,\ell})\} \to E(g^{k,*})$ holds. Let $g^{k,*}$ be a limit point of $g^{k,\ell}$. There exists a subsequence $\{g^{k,\ell_j}\}$ of $\{g^{k,\ell}\}$ converging to $g^{k,*}$. By the second property in [41, Proposition 5], there exists a sequence $\xi_g^{k,\ell+1} \in \partial E(g^{k,\ell+1})$ satisfying the second inequality in [41, Proposition 5]. Due to (B), $\xi_g^{k,\ell}$ decays to $\mathbf{0}$ as $\ell \to \infty$, and then, ξ_g^{k,ℓ_j} also converges to $\mathbf{0}$ as ℓ goes to ∞. Owing to closedness [39, Remark 2.1 (b)] of ∂E and the third property of [41, Proposition 5], $\mathbf{0} \in \partial E(g^{k,*})$. Thus, $g^{k,*}$ is a stationary point of the g-subproblem. □

The subproblem (4.9) for the variable $g^{k,\ell+1}$ is considered next. Although this subproblem is convex, it contains the nondifferentiable term $\gamma\langle w_1^{k,\ell+1}, |\nabla g|\rangle$. By employing the variable splitting technique [49], the subproblem can be reformulated as the following constrained minimization problem:

$$\begin{aligned} &\min_{g,d,z,t_i} \mu \sum_{\Omega} G(z) + \lambda \sum_{i=1}^{K} \sum_{\Omega} (t_i)^2 u_i^k + \mathcal{I}_{S_1}(z) + \frac{\delta}{2}\|g - g^k\|_2^2 + \gamma\langle w_1^{k,\ell+1}, |d|\rangle, \\ &\text{s.t.} \quad d = \nabla g, \quad z = Ag, \quad t_i = g - c_i^k, \quad i = 1, \ldots, K. \end{aligned} \tag{4.10}$$

Various optimization algorithms for the linearly constrained convex minimization were proposed, such as the ADMM [50] and the primal-dual algorithm [51]. Here, ADMM, a well-known algorithm for solving linearly constrained optimization problems, is utilized. The augmented Lagrangian function of problem (4.10) is given by

$$\begin{aligned} \mathcal{L}(g, d, z, t_i, a_d, a_z, a_i^t; \nu) = {} & \mu \sum_{\Omega} G(z) + \lambda \sum_{i=1}^{K} \sum_{\Omega} (t_i)^2 u_i^k + \mathcal{I}_{S_1}(z) + \frac{\delta}{2}\|g - g^k\|_2^2 \\ & + \gamma\langle w_1^{k,\ell+1}, |d|\rangle - \langle a_d, d - \nabla g\rangle + \frac{\nu}{2}\|d - \nabla g\|_2^2 - \langle a_z, z - Ag\rangle \\ & + \frac{\nu}{2}\|z - Ag\|_2^2 - \sum_{i=1}^{K} \langle a_i^t, t_i - g + c_i^k\rangle + \frac{\nu}{2} \sum_{i=1}^{K} \|t_i - g + c_i^k\|_2^2. \end{aligned} \tag{4.11}$$

where $a_d, a_z, a_i^t, i = 1, \cdots, K$ are the Lagrange multipliers defined on Ω, and ν is a penalty parameter. The ADMM alternately minimizes the augmented Lagrangian function with respect to one variable, whereas the other variables are fixed, and the Lagrange multipliers are then updated according to the primal-dual theory.

The ADMM can be applied to problem (4.10), resulting in the following iterative algorithm:

$$\begin{aligned} &\begin{pmatrix} d^{m+1} \\ z^{m+1} \\ t_i^{m+1} \end{pmatrix} := \arg\min_{d,z,t_i} \ \mathcal{L}(g^m, d, z, t_i, a_d^m, a_z^m, (a_i^t)^m; \nu), \\ &g^{m+1} := \arg\min_{g} \ \mathcal{L}(g, d^{m+1}, z^{m+1}, t_i^{m+1}, a_d^m, a_z^m, (a_i^t)^m; \nu) \\ &a_d^{m+1} = a_d^m - \nu(d^{m+1} - \nabla g^{m+1}) \\ &a_z^{m+1} = a_z^m - \nu(z^{m+1} - Ag^{m+1}) \\ &(a_i^t)^{m+1} = (a_i^t)^m - \nu(t_i^{m+1} - g^{m+1} + c_i^k). \end{aligned}$$

Because problem (4.10) is a convex minimization with linear constraints, the convergence results of ADMM for (4.10) can be directly applied according to [50]. First, the subproblem for $(d^{m+1}, z^{m+1}, t_i^{m+1})$ can be solved independently as follows:

$$\begin{aligned} d^{m+1} &= \arg\min_d \gamma\langle w_1^{k,\ell+1}, |d|\rangle - \langle a_d^m, d - \nabla g^m\rangle + \frac{\nu}{2}\|d - \nabla g^m\|_2^2, \\ z^{m+1} &= \arg\min_z \mu \sum_\Omega G(z) + \mathcal{I}_{S_1}(z) + \langle a_z^m, z - Ag^k\rangle + \frac{\nu}{2}\|z - Ag^m\|_2^2, \\ t_i^{m+1} &= \arg\min_{t_i} \lambda \sum_\Omega (t_i)^2 u_i^k - \langle (a_i^t)^m, t_i - g^m + c_i^k\rangle + \frac{\nu}{2}\|t_i - g^m + c_i^k\|_2^2. \end{aligned}$$

The (d, t_i)-minimization problems are also solved as exactly:

$$\begin{aligned} d^{m+1} &= shrink(\nabla g^m + \frac{a_d^m}{\nu}, \frac{\gamma w_1^{k,\ell+1}}{\nu}), \\ t_i^{m+1} &= \frac{(a_i^t)^m + \nu(g^m - c_i^k)}{2\lambda u_i^k + \nu}, \quad i = 1, \cdots, K, \end{aligned}$$

where *shrink* is defined as

$$shrink(a, b) = \frac{a}{|a|} \cdot \max(|a| - b, 0). \tag{4.12}$$

The z-subproblem can be solved easily using Newton's method:

$$z_{l+1}^{m+1} = \min\left(255, \max\left(0, z_l^{m+1} - \frac{\bar{G}(z_l^{m+1})}{\bar{G}'(z_l^{m+1})}\right)\right),$$

where

$$\bar{G}(z) = \mu \sum_\Omega G(z) + \langle a_z^m, z - Ag^m\rangle + \frac{\nu}{2}\|z - Ag^m\|_2^2.$$

Finally, the solution of the g-subproblem can be obtained by solving the following normal equation:

$$(\nu A^T A + \delta I + \nu \nabla^T \nabla + \nu K I) g^{m+1} = rhs_g, \tag{4.13}$$

where

$$rhs_g = \nabla^T(\nu d^{m+1} - a_d^m) + A^T(\nu z^{m+1} - a_z^m) + \sum_{i=1}^K (-(a_i^t)^m + \nu(t_i^{m+1} + c_i^k)) + \delta g^k.$$

If A is a double symmetric blurring operator, the matrix $\nu A^T A + \delta I + \nu \nabla^T \nabla + \nu K I$ can be diagonalized using a two-dimensional discrete cosine transform (DCT2) under a symmetric boundary condition. This allows the solution to Eq (4.13) to be expressed as

$$g^{m+1} = \mathcal{D}^{-1}\left(\frac{\mathcal{D}(rhs_g)}{(\nu K + \delta)\mathcal{D}(I) + \nu\mathcal{D}(\nabla^T \nabla) + \nu\mathcal{D}(K^T K)}\right).$$

Algorithm 1 The proposed algorithm

Input: choose the parameters λ, μ, γ, δ, η, ρ, the maximum numbers of iterations N_1, N_2.
Initialization: let $g^0 = f$, c_i^0, u_i^0 = the result of FCM2 with initial f.
repeat
  Compute g^{k+1} by iterating for $\ell = 0, 1, 2, \cdots, N_1$:
    $w_1^{k,\ell+1} = \dfrac{1}{1+\rho|\nabla g^\ell|}$,
    $d^{\ell+1} = shrink(\nabla g^\ell + \frac{a_d^\ell}{\delta}, \frac{\gamma w_1^{k,\ell+1}}{\delta})$,
    $t_i^{\ell+1} = \frac{(a_i^t)^\ell + \delta(g^\ell - c_i^k)}{2u_i^k + \delta}, \quad i = 1, \cdots, K$,
    Compute $z^{\ell+1}$by iterating of Newton's method for $l = 0, 1, \cdots, N_3$:
      $z^{l+1} = \min\left(255, \max\left(0, z^l - \dfrac{\bar{G}(z^l)}{\bar{G}'(z^l)}\right)\right)$,
    $g^{\ell+1} = \mathcal{D}^{-1}\left(\frac{\mathcal{D}(rhs_g)}{\delta K\mathcal{D}(I)+\delta\mathcal{D}(\nabla^T\nabla)+\delta\mathcal{D}(K^TK)}\right)$,
    $a_d^{\ell+1} = a_d^\ell - \delta(d^{\ell+1} - \nabla g^{\ell+1})$,
    $a_z^{\ell+1} = a_z^\ell - \delta(z^{\ell+1} - Ag^{\ell+1}$,
    $(a_i^t)^{\ell+1} = (a_i^t)^\ell - \delta(t_i^{\ell+1} - g^{\ell+1} + c_i^k), \quad i = 1, \cdots, K$.
  Compute c_i^{k+1} by the formula
$$c_i^{k+1} = \min\left(255, \max\left(0, \frac{2\lambda\sum_\Omega g^{k+1}u_i^k + \delta c_i^k}{2\lambda\sum_\Omega u_i^k + \delta}\right)\right), \quad i = 1, \cdots, K.$$
  Compute u_i^{k+1} by iterating for $\ell = 0, 1, 2, \cdots, N_2$:
    $w_{2,i}^{k,\ell+1} = \frac{1}{1+\rho|\nabla u_i^\ell|}, \quad i = 1, \cdots, K$,
    $p_i^{\ell+1} = proj_S(u_i^\ell + \frac{b_i^\ell}{\eta}), \quad i = 1, \cdots, K$,
    $h_i^{\ell+1} = shrink(\nabla u_i^\ell + \frac{r_i^\ell}{\eta}, \frac{w_{2,i}^{k,\ell+1}}{\eta}), \quad i = 1, \cdots, K$,
    $u_i^{\ell+1} = \mathcal{D}^{-1}\left(\frac{\mathcal{D}(rhs_u)}{\eta\mathcal{D}(I)+\eta\mathcal{D}(\nabla^T\nabla)}\right), \quad i = 1, \cdots, K$,
    $b_i^{\ell+1} = b_i^\ell - \eta(p_i^{\ell+1} - u_i^{\ell+1}), \quad i = 1, \cdots, K$,
    $r_i^{\ell+1} = r_i^\ell - \eta(h_i^{\ell+1} - \nabla u_i^{\ell+1}), \quad i = 1, \cdots, K$.
until the stopping condition is satisfied.
Output: u_i for $i = 1, \cdots, K$.

4.3. Iterative algorithm for the u_i-subproblem

In this subsection, the author provides the proposed algorithm for solving the u_i-subproblem. In a way similar to that described in the previous subsection, IRL1 can be applied to the u_i-subproblem in (4.2), which gives rise to the following iterative algorithm:

$$\begin{aligned} w_{2,i}^{k,\ell+1} &= \frac{1}{1+\rho|\nabla u_i^\ell|}, \\ u_i^{k,\ell+1} &:= \arg\min_u \ \lambda\sum_{i=1}^K\sum_\Omega (g^{k+1} - c_i^{k+1})^2 u_i + \sum_{i=1}^K \langle w_{2,i}^{k,\ell+1}, |\nabla u_i|\rangle + \mathcal{I}_S(u_1, \cdots, u_K) \end{aligned} \tag{4.14}$$

$$+\frac{\delta}{2}\sum_{i=1}^{K}\|u_i-u_i^k\|_2^2.$$

It can be demonstrated that the convergence result of the IRL1 (4.14) is obtained in a similar manner to that described in Theorem 4.2.

Problem (4.14) is a convex minimization problem with a nondifferentiable term. Hence, the following equivalent constrained minimization is considered:

$$\begin{aligned}\min_{u_i,p_i,h_i}\quad & \lambda\sum_{i=1}^{K}\sum_{\Omega}(g^{k+1}-c_i^{k+1})^2u_i+\sum_{i=1}^{K}\langle w_{2,i}^{k,\ell+1},|h_i|\rangle+\mathcal{I}_S(p_1,\cdots,p_K)+\frac{\delta}{2}\sum_{i=1}^{K}\|u_i-u_i^k\|_2^2 \quad (4.15)\\ \text{s.t.}\quad & p_i=u_i, h_i=\nabla u_i,\quad i=1,\cdots,K.\end{aligned}$$

ADMM is applied to problem (4.15), yielding

$$\begin{aligned}\begin{pmatrix}p_i^{m+1}\\ h_i^{m+1}\end{pmatrix} &:= \arg\min_{p_i,h_i}\Big\{\sum_{i=1}^{K}\langle w_{2,i}^{k,\ell+1},|h_i|\rangle+\mathcal{I}_S(p_1,\cdots,p_K)-\sum_{i=1}^{K}\langle b_i^m,p_i\rangle\\ &\quad+\sum_{i=1}^{K}\frac{\eta}{2}\|p_i-u_i^m\|_2^2-\sum_{i=1}^{K}\langle r_i^m,h_i\rangle+\sum_{i=1}^{K}\frac{\eta}{2}\|h_i-\nabla u_i^m\|_2^2\Big\}, \quad (4.16)\\ u_{i+1}^k &:= \arg\min_{u}\Big\{\langle(g^{k+1}-c_i^{k+1})^2,u_i\rangle+\langle b_i^m,u_i\rangle+\frac{\eta}{2}\|u_i-p_i^{m+1}\|_2^2+\langle r_i^m,\nabla u_i\rangle\\ &\quad+\frac{\eta}{2}\|\nabla u_i-h_i^{m+1}\|_2^2+\frac{\delta}{2}\|u_i-u_i^k\|_2^2\Big\},\ i=1,\cdots,K, \quad (4.17)\\ b_i^{m+1} &= b_i^m-\eta(p_i^{m+1}-u_i^{m+1}),\quad i=1,\cdots,K\\ r_i^{m+1} &= r_i^m-\eta(h_i^{m+1}-\nabla u_i^{m+1}),\quad i=1,\cdots,K.\end{aligned}$$

The variables in the (p_i,h_i)-subproblem (4.16) are decoupled, so they can be solved separately as

$$\begin{aligned}p_i^{m+1} &= proj_S(u_i^m+\frac{b_i^m}{\eta}),\\ h_i^{m+1} &= shrink(\nabla u_i^m+\frac{r_i^m}{\eta},\frac{w_{2,i}^{k,\ell+1}}{\eta})\end{aligned}$$

for each $i=1,\cdots,K$, where $proj_S$ is the projection onto simplex S for which the specific formula is given in [52].

In (4.17), the u_i-subproblem is a least-squares problem, so its solution u_i^{m+1} can be obtained by solving the following normal equation:

$$(\eta I+\eta\nabla^T\nabla+\delta I)u_i = rhs_u, \quad (4.18)$$

where

$$rhs_u = -(g^{k+1}-c_i^{k+1})^2+(\eta p_i^{m+1}-b_i^m)+\nabla^T(\eta h_i^{m+1}-r_i^m)+\delta u_i^k.$$

Hence, by taking the DCT2, we obtain the exact solution u_i^{m+1} of the problem (4.18).

ADMM typically requires multiple iterations to ensure convergence. However, for each IRL1 step, only a single iteration of ADMM is performed to maintain computational efficiency, which is sufficient in practice. In summary, Algorithm 1 presents the complete procedure for solving the proposed model (4.1).

5. Numerical results

In this section, the author presents numerical results obtained using the proposed model and compares them with several representative existing models. The CV model [10] is a region-based active contour approach that performs image segmentation without relying on explicit edge information. The fuzzy C-means clustering with level set method (FCMLSM) [53] integrates spatial fuzzy clustering with level set evolution and has been widely applied to medical image segmentation. The Chen model [29] is a variational segmentation framework that explicitly accounts for Rician noise through an image restoration formulation.

All models were tested on several synthetic and real images, including examples from the dataset in [54]. All test images are shown in Figure 2. Segmentation performance is evaluated using accuracy, precision, recall, F-measure, and intersection over union (IoU), whose detailed definitions and corresponding MATLAB implementations are provided in [55]. All numerical experiments were conducted on a 64-bit macOS system using a MacBook Pro equipped with an Intel Core i9 CPU at 2.40 GHz and 32 GB of RAM.

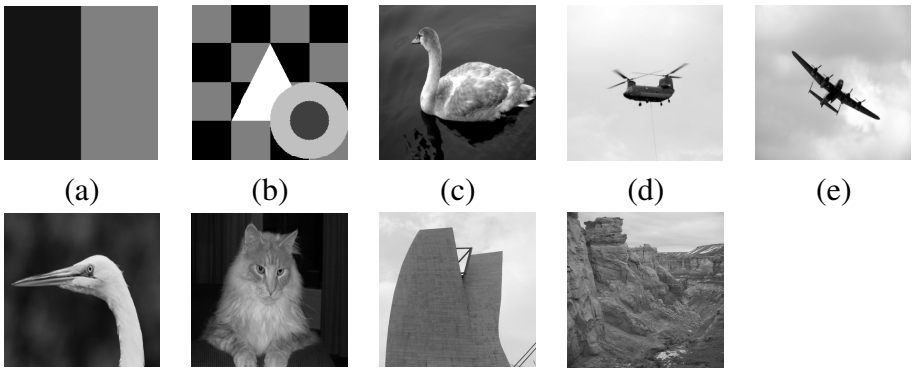

Figure 2. Test images used in the experiments: (a) syn2 (128×128), (b) syn5 (235×237), (c) 113334665744 (300×225), (d) b2chopper008 (300×225), (e) bbmf (300×225), (f) egret face (300×200), (g) oscar (300×225), (h) guggenheim (300×400), (i) mountain (512×683).

5.1. Implementation setting

The proposed algorithm is terminated when the following stopping criterion is satisfied:

$$\frac{\sqrt{\sum_{i=1}^{K}(c_i^k - c_i^{k-1})^2}}{\sqrt{\sum_{i=1}^{K}(c_i^{k-1})^2}} \leq \text{tol} \quad \text{or} \quad k > 50,$$

where the tolerance is set to tol = 0.1. The parameter settings used in the numerical experiments are as follows. The parameters (γ, λ, μ) were tuned to obtain visually satisfactory results as well as favorable quantitative performance. The parameter ρ in the nonconvex logarithmic regularization was fixed at 0.01, and the penalty parameters in the numerical solvers were set to $(\delta, \eta) = (1, 100)$. The maximum numbers of iterations for updating g and u_i were fixed at $N_1 = N_2 = 10$, and the maximum number of iterations for Newton's method was set to $N_3 = 5$. The following parameter ranges were considered: $\gamma \in \{5, 10, 15, 30, 50, 100\}$, $\lambda \in \{0.01, 0.1\}$, and $\mu \in \{100, 500, 1000\}$.

Because the proposed model is nonconvex, the results are sensitive to the initialization of c_i and u_i. The initial values of c_i were obtained using the fuzzy C-means method [56]. For two-phase segmentation, the initial u_i were generated using circular level sets over the image domain, whereas for multiphase segmentation, they were initialized using the fuzzy C-means method.

Three types of blurring operators were considered: Gaussian blur with a window size of 10 and standard deviation 10, motion blur with length 15 and angle 60°, and uniform blur. For two-phase segmentation, the window size of the uniform blur was set to 3, whereas for multiphase segmentation it was set to 5. The observed image f was generated by first applying the blurring operator A and then adding Rician noise with $\sigma = 15$ for two-phase segmentation and $\sigma = 5$ for multiphase segmentation.

Because motion blur is not doubly symmetric, the DCT-based solver cannot be applied. In this case, the restoration and segmentation results were obtained using the two-dimensional fast Fourier transform under symmetric boundary conditions, following the approach in [57]. For the sake of reproducibility, the MATLAB codes used in the numerical experiments are available at `https://buly.kr/8phgkh4`.

5.2. *Sensitivity and influence of parameters*

This subsection investigates the effect of the model parameters μ, λ, and γ via a single-parameter sensitivity analysis, where one parameter is varied while the others remain fixed. Unless stated otherwise, the sensitivity analysis is conducted under the Gaussian blur.

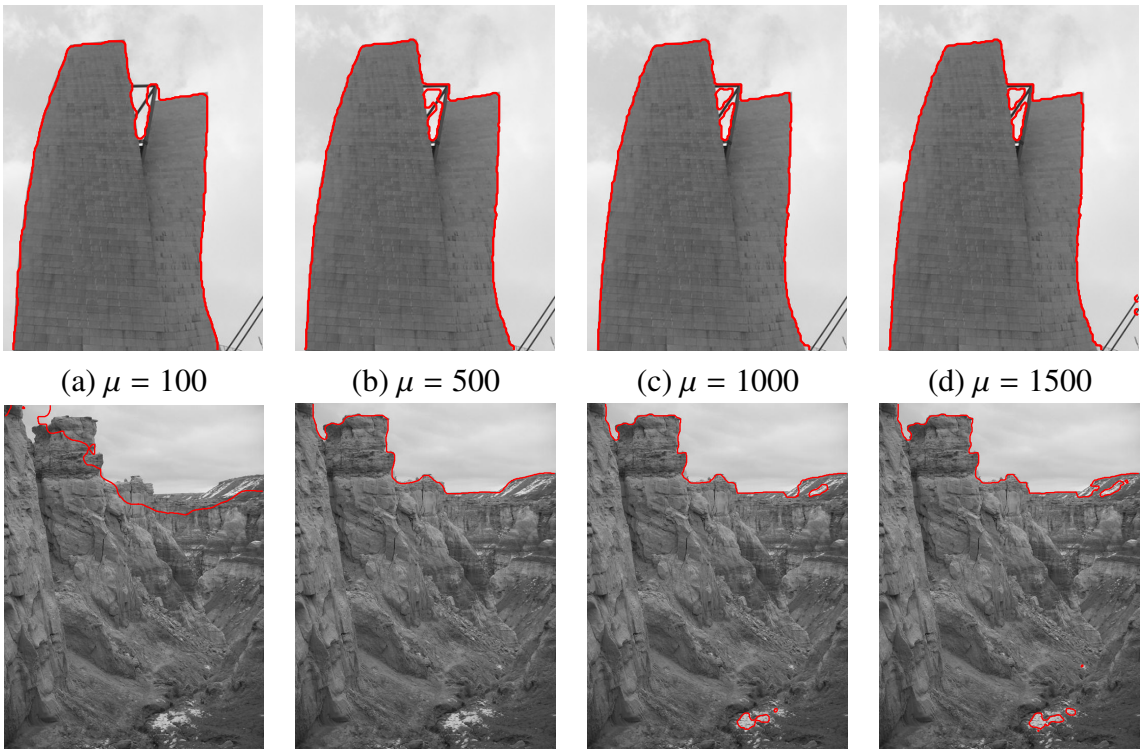

(a) $\mu = 100$ (b) $\mu = 500$ (c) $\mu = 1000$ (d) $\mu = 1500$

(a) $\mu = 10$ (b) $\mu = 100$ (c) $\mu = 500$ (d) $\mu = 1000$

Figure 3. Sensitivity and influence analysis with respect to μ, with all other parameters fixed. Top row: segmentation results for the guggenheim image. Bottom row: segmentation results for the mountain image.

Sensitivity and influence with respect to μ: The parameter μ controls the strength of the data fidelity term and is critical for compensating for noise and blur. Experiments were conducted with $\mu \in \{10, 100, 500, 1000, 1500\}$. Figure 3 presents the segmentation results for different values of μ. For small values (e.g., $\mu = 100$), the data fidelity term becomes too weak, leading to oversmoothing and preventing accurate capture of fine building structures.

As μ increases, building boundaries are better preserved. However, when $\mu = 1500$, thin structures unrelated to the true building boundary are incorrectly detected.

A similar trend is observed in the second test image, where the best segmentation performance occurs at $\mu = 100$. Overall, the parameter μ exhibits moderate sensitivity. Based on these observations, μ is tuned within the range $\mu \in \{100, 500, 1000\}$.

Sensitivity and influence with respect to λ: The parameter λ weights the data fitting term that enforces alignment of the segmentation curve with the target object. The values tested were $\lambda \in \{0.001, 0.01, 0.1, 0.5\}$. The corresponding segmentation results are shown in Figure 4. When $\lambda = 0.001$, the data fidelity term is too weak, resulting in insufficient object fitting and segmentation failure. For $\lambda = 0.01$ and $\lambda = 0.1$, satisfactory and visually similar segmentation results are obtained. In contrast, when $\lambda = 0.5$, the overly strong data fidelity term weakens the regularization effect on the segmentation curve length, leading to the inclusion of noise. Overall, these results indicate that λ is not highly sensitive, as the segmentation results remain stable once λ is chosen within a reasonable and practically relevant range. Accordingly, λ is selected from the range $\lambda \in \{0.01, 0.1\}$.

(a) $\lambda = 0.001$ (b) $\lambda = 0.01$ (c) $\lambda = 0.1$ (d) $\lambda = 0.5$

Figure 4. Sensitivity and influence analysis with respect to λ, with all other parameters fixed.

Sensitivity and influence with respect to γ: The parameter γ controls the strength of the regularization for noise suppression and blur compensation. Experiments were conducted with $\gamma \in \{1, 5, 30, 50, 100, 150\}$. Figure 5 presents the segmentation results for two test images.

In the first image, when $\gamma = 1$, the regularization is insufficient, causing the segmentation to include both the target object (aircraft) and background noise. As γ increases, noise is gradually suppressed, and the target object is more clearly segmented. However, for large values of γ (e.g., $\gamma > 100$), excessive regularization leads to blurred object boundaries. In this case, $\gamma = 5$ achieves the best balance between noise suppression and boundary preservation.

A similar behavior is observed in the second image. For relatively small values of γ (e.g., 5, 30), undesired artifacts such as fine cracks within the mountain region appear. This phenomenon is attributed to the abundance of fine details in mountainous textures.

The most satisfactory result is obtained at $\gamma = 100$. Further increasing γ to 150 causes distortion of the boundary between the mountain and the sky. Overall, γ is found to be the most sensitive parameter among the three. Based on these observations, γ is tuned within the range $\gamma \in \{5, 10, 15, 30, 50, 100\}$.

For all competing variational methods, parameters were tuned following the recommendations in

the original papers to achieve their best performance.

(a) $\gamma = 1$ (b) $\gamma = 5$ (c) $\gamma = 30$ (d) $\gamma = 100$

(a) $\gamma = 5$ (b) $\gamma = 30$ (c) $\gamma = 100$ (d) $\gamma = 150$

Figure 5. Sensitivity and influence analysis with respect to γ, with all other parameters fixed. Top row: segmentation results for the b2chopper008 image. Bottom row: segmentation results for the mountain image.

5.3. Segmentation results

First, the numerical results of segmenting synthetic images will be analyzed in Figures 6–8. The quantitative evaluation of segmentation performance is reported in Tables 1–3. For the CV and FCMLSM models, the object boundaries are not accurately detected because these models do not incorporate a mechanism for blur removal. The original image in Figure 9 consists of five phases. Thus, the CV model requires three level set functions, which can generate up to eight regions. Due to the presence of blur in the observed image, parts of the square boundaries are incorrectly assigned to the additional regions. In contrast, as shown in Figure 6, both the Chen model and the proposed model achieve nearly perfect segmentation results, owing to the inclusion of a term that explicitly accounts for image blur. In the multiphase case, the proposed model demonstrates a superior ability to segment the boundaries of triangles and squares compared to the Chen model, yielding results that are closer to the ground truth.

Figure 10 presents the results of two-phase segmentation for a natural image corrupted by Rician noise with $\sigma = 15$ and blur. It is observed that the CV model captures the building boundaries in a jagged manner in all cases. Because the CV model does not include a mechanism to suppress Rician noise, it tends to falsely detect noise as object boundaries. The FCMLSM model produces unsatisfactory results under Gaussian and motion blur, leading to inaccurate and less smooth boundaries. The Chen model successfully captures the overall shape of the building in all three cases.

However, it fails to accurately detect sharp corners and the boundaries between adjacent buildings. In contrast, the proposed model provides the most accurate and consistent boundary detection across

all cases. In particular, it precisely identifies the slender structure located in the central area of the building.

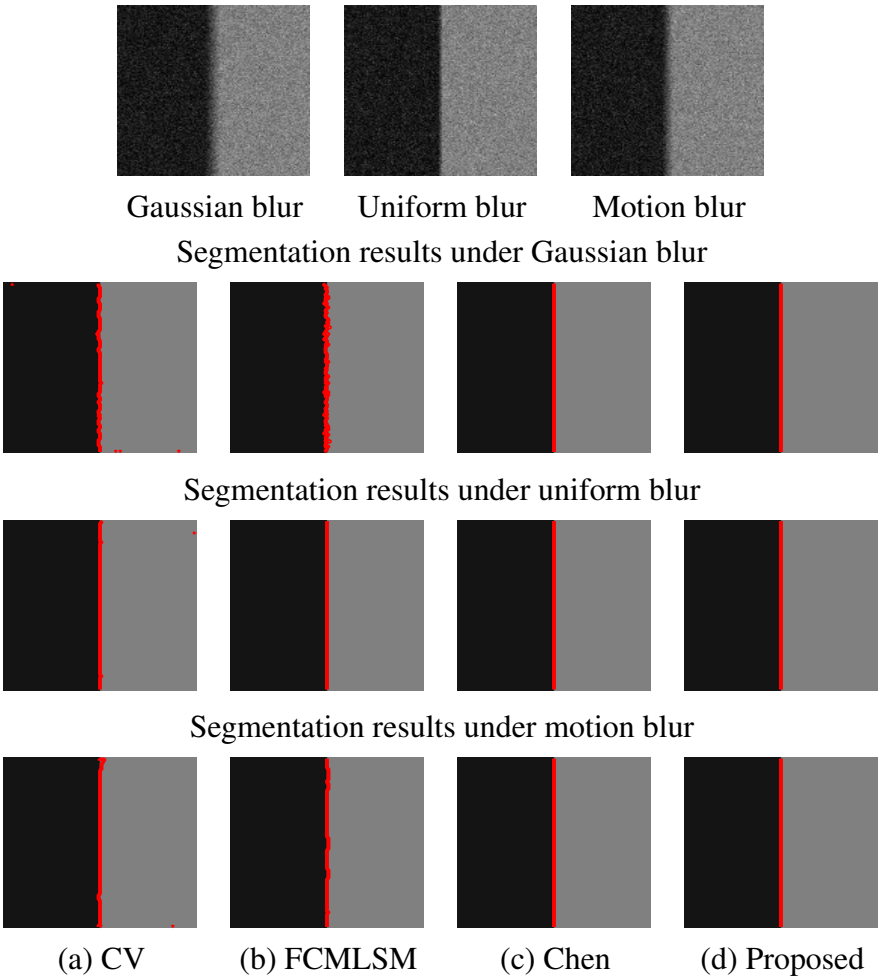

Figure 6. Segmentation results of a synthetic image under different blur kernels. Top row: blurred and noisy input images. Second to fourth rows: segmentation results under Gaussian blur, uniform blur, and motion blur, respectively. Columns correspond to CV [10], FCMLSM [53], Chen [29], and the proposed method.

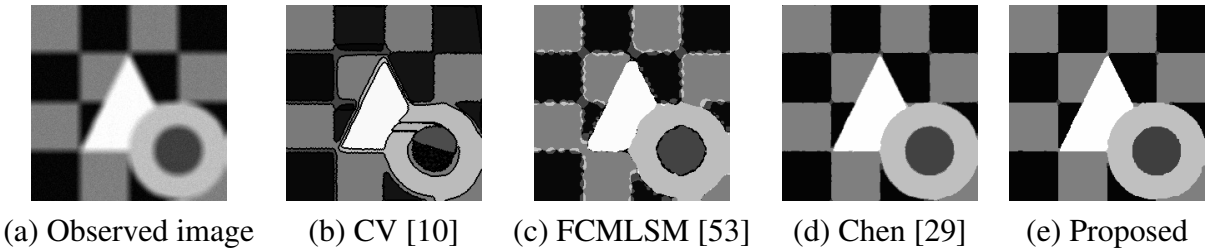

Figure 7. Segmentation results for a synthetic image corrupted by Gaussian blur and Rician noise. (a) Observed image and approximated images obtained by (b) CV [10], (c) FCMLSM [53], (d) Chen [29], and (e) the proposed method.

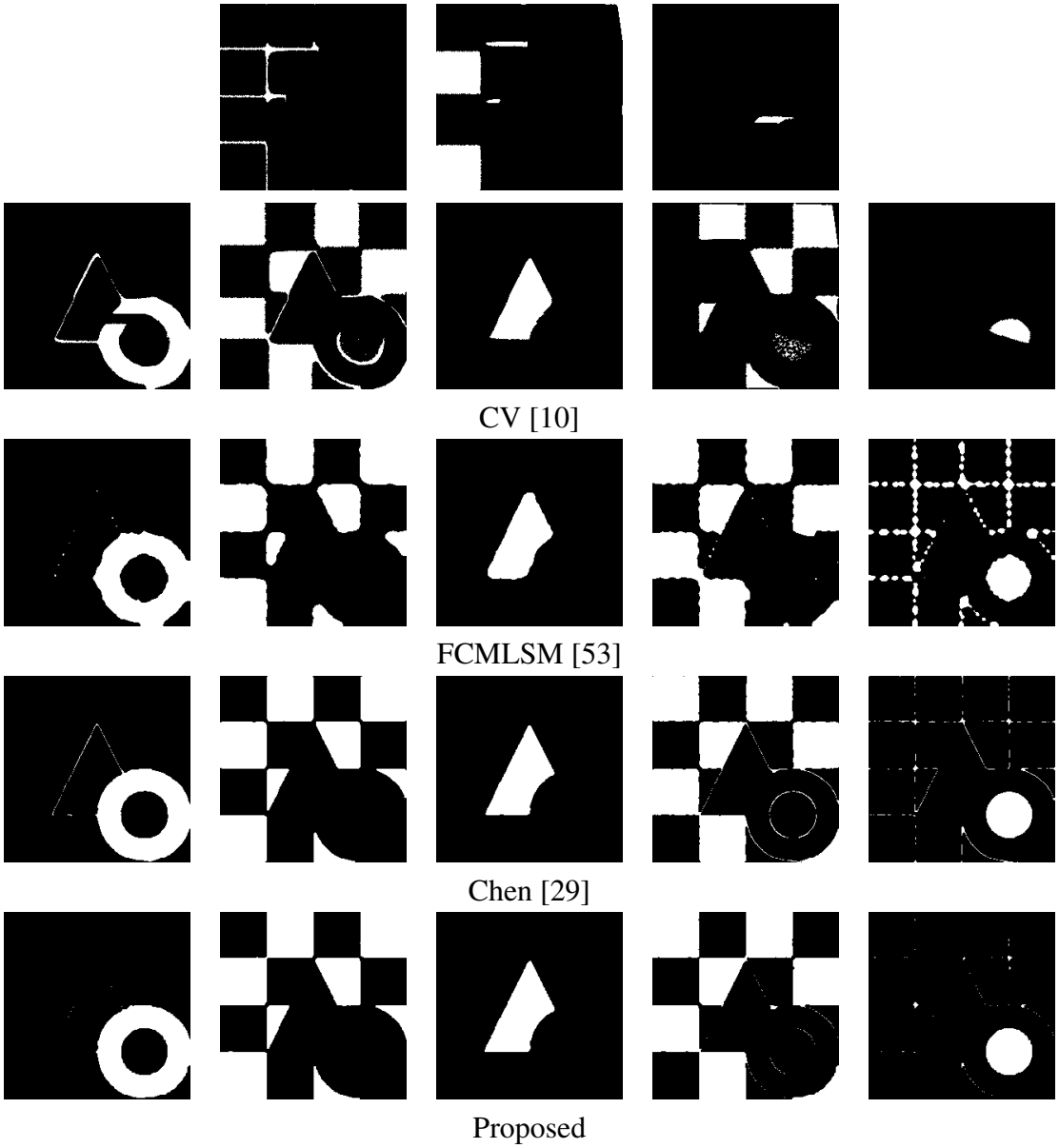

Figure 8. Visualization of the five-phase segmentation results corresponding to Figure 7.

Table 1. Quantitative segmentation results under Gaussian blur.

Image	Model	Accuracy	F-measure	Precision	Recall	IoU
syn2	CV	0.9970	0.9970	0.9970	0.9970	0.9940
	FCMLSM	0.9946	0.9946	0.9946	0.9946	0.9892
	Chen	**1.0000**	**1.0000**	**1.0000**	**1.0000**	**1.0000**
	Proposed	**1.0000**	**1.0000**	**1.0000**	**1.0000**	**1.0000**
syn5	CV	0.8662	0.7644	0.9615	0.6642	0.6405
	FCMLSM	0.9243	0.9072	0.9204	0.9019	0.8384
	Chen	0.9782	0.9619	0.9524	0.9747	0.9296
	Proposed	**0.9930**	**0.9885**	**0.9857**	**0.9915**	**0.9775**
113334665744	CV	0.9418	0.9166	0.9427	0.8963	0.8494
	FCMLSM	0.9278	0.8922	0.9432	0.8596	0.8110
	Chen	0.9313	0.8982	0.9453	0.8671	0.8202
	Proposed	**0.9495**	**0.9274**	**0.9561**	**0.9054**	**0.8672**
b2chopper008	CV	0.6384	0.3899	0.4634	0.3374	0.3193
	FCMLSM	0.9827	0.8950	0.9791	0.8379	0.8237
	Chen	0.9866	0.9218	**0.9827**	0.8758	0.8631
	Proposed	**0.9885**	**0.9381**	0.9573	**0.9206**	**0.8886**
bbmf	CV	0.9881	0.9421	0.9516	0.9331	0.8951
	FCMLSM	0.9885	0.9423	0.9706	0.9176	0.8954
	Chen	0.9903	0.9511	**0.9816**	0.9247	0.9101
	Proposed	**0.9909**	**0.9566**	0.9580	**0.9553**	**0.9195**
egret face	CV	0.9684	0.9450	0.9726	0.9222	0.8979
	FCMLSM	0.9705	0.9488	0.9751	0.9269	0.9045
	Chen	0.9689	0.9455	**0.9773**	0.9200	0.8988
	Proposed	**0.9803**	**0.9669**	0.9767	**0.9577**	**0.9367**
oscar	CV	0.9572	0.9560	0.9640	0.9515	0.9158
	FCMLSM	0.9444	0.9426	0.9546	0.9368	0.8916
	Chen	0.9566	0.9554	0.9640	0.9507	0.9148
	Proposed	**0.9637**	**0.9628**	**0.9684**	**0.9592**	**0.9283**
guggenheim	CV	0.9859	0.9857	0.9850	0.9865	0.9718
	FCMLSM	0.9843	0.9841	0.9831	0.9853	0.9687
	Chen	0.9881	0.9879	0.9868	0.9893	0.9762
	Proposed	**0.9893**	**0.9892**	**0.9882**	**0.9903**	**0.9786**
mountain	CV	0.9904	0.9825	0.9751	0.9902	0.9658
	FCMLSM	0.9903	0.9823	0.9727	0.9926	0.9655
	Chen	0.9916	0.9846	0.9759	0.9939	0.9699
	Proposed	**0.9962**	**0.9930**	**0.9897**	**0.9963**	**0.9861**

*The best segmentation performance is indicated in bold, and the second-best is underlined when applicable.

Table 2. Quantitative segmentation results under uniform blur.

Image	Model	Accuracy	F-measure	Precision	Recall	IoU
syn2	CV	0.9998	0.9998	0.9998	0.9998	0.9995
	FCMLSM	1.0000	1.0000	1.0000	1.0000	1.0000
	Chen	**1.0000**	**1.0000**	**1.0000**	**1.0000**	**1.0000**
	Proposed	**1.0000**	**1.0000**	**1.0000**	**1.0000**	**1.0000**
syn5	CV	0.8085	0.8092	0.8444	0.8504	0.7217
	FCMLSM	0.9635	0.9634	0.9795	0.9484	0.9298
	Chen	0.9905	0.9836	0.9809	0.9867	0.9682
	Proposed	**0.9976**	**0.9960**	**0.9953**	**0.9968**	**0.9921**
113334665744	CV	0.9388	0.9090	0.9586	0.8765	0.8374
	FCMLSM	0.9205	0.8774	0.9517	0.8368	0.7891
	Chen	0.9412	0.9129	0.9601	0.8814	0.8437
	Proposed	**0.9471**	**0.9229**	**0.9610**	**0.8956**	**0.8598**
b2chopper008	CV	0.9896	0.9404	0.9914	0.8999	0.8925
	FCMLSM	0.9881	0.9310	0.9924	0.8843	0.8773
	Chen	0.9887	0.9347	**0.9936**	0.8895	0.8833
	Proposed	**0.9920**	**0.9555**	0.9884	**0.9272**	**0.9177**
bbmf	CV	0.9889	0.9418	0.9932	0.9010	0.8946
	FCMLSM	0.9868	0.9293	0.9931	0.8815	0.8746
	Chen	0.9884	0.9389	**0.9936**	0.8962	0.8900
	Proposed	**0.9940**	**0.9701**	0.9934	**0.9493**	**0.9433**
egret face	CV	0.9701	0.9474	0.9820	0.9200	0.9021
	FCMLSM	0.9619	0.9315	0.9776	0.8976	0.8752
	Chen	0.9727	0.9521	0.9834	0.9267	0.9103
	Proposed	**0.9750**	**0.9565**	**0.9849**	**0.9330**	**0.9180**
oscar	CV	0.9564	0.9552	0.9633	0.9506	0.9143
	FCMLSM	0.9535	0.9522	0.9616	0.9472	0.9089
	Chen	0.9562	0.9550	0.9638	0.9502	0.9140
	Proposed	**0.9621**	**0.9612**	**0.9682**	**0.9570**	**0.9253**
guggenheim	CV	0.9858	0.9857	0.9848	0.9867	0.9717
	FCMLSM	0.9856	0.9854	0.9846	0.9864	0.9713
	Chen	0.9875	0.9873	0.9862	0.9888	0.9750
	Proposed	**0.9897**	**0.9895**	**0.9885**	**0.9908**	**0.9793**
mountain	CV	0.9904	0.9824	0.9743	0.9910	0.9657
	FCMLSM	0.9890	0.9800	0.9689	0.9921	0.9611
	Chen	**0.9963**	**0.9931**	**0.9898**	**0.9965**	**0.9863**
	Proposed	0.9950	0.9907	0.9857	0.9959	0.9817

*The best segmentation performance is indicated in bold, and the second-best is underlined when applicable.

Table 3. Quantitative segmentation results under motion blur.

Image	Model	Accuracy	F-measure	Precision	Recall	IoU
syn2	CV	0.9987	0.9987	0.9987	0.9987	0.9974
	FCMLSM	0.9981	0.9981	0.9981	0.9981	0.9962
	Chen	**1.0000**	**1.0000**	**1.0000**	**1.0000**	**1.0000**
	Proposed	**1.0000**	**1.0000**	**1.0000**	**1.0000**	**1.0000**
syn5	CV	0.7411	0.6913	0.7590	0.6535	0.5973
	FCMLSM	0.9139	0.8938	0.9157	0.8791	0.8163
	Chen	0.9791	0.9627	0.9514	0.9782	0.9315
	Proposed	**0.9957**	**0.9931**	**0.9914**	**0.9949**	**0.9864**
113334665744	CV	0.9404	0.9139	0.9451	0.8905	0.8449
	FCMLSM	0.9222	0.8818	0.9443	0.8451	0.7955
	Chen	0.9322	0.8979	**0.9562**	0.8621	0.8200
	Proposed	**0.9542**	**0.9259**	0.9500	**0.9237**	**0.8815**
b2chopper008	CV	0.9821	0.9020	0.9273	0.8798	0.8334
	FCMLSM	0.9824	0.8974	0.9556	0.8536	0.8271
	Chen	0.9870	0.9250	**0.9799**	0.8824	0.8680
	Proposed	**0.9875**	**0.9325**	0.9511	**0.9156**	**0.8797**
bbmf	CV	0.9817	0.9192	0.8911	**0.9524**	0.8585
	FCMLSM	0.9846	0.9268	0.9280	0.9255	0.8704
	Chen	0.9909	0.9545	**0.9787**	0.9330	0.9159
	Proposed	**0.9918**	**0.9599**	0.9707	0.9497	**0.9252**
egret face	CV	0.9671	0.9426	0.9705	0.9197	0.8938
	FCMLSM	0.9627	0.9336	0.9730	0.9034	0.8786
	Chen	0.9675	0.9430	**0.9742**	0.9179	0.8946
	Proposed	**0.9788**	**0.9649**	0.9668	**0.9630**	**0.9330**
oscar	CV	0.9525	0.9512	0.9599	0.9465	0.9071
	FCMLSM	0.9415	0.9396	0.9525	0.9336	0.8863
	Chen	0.9554	0.9542	0.9631	0.9493	0.9125
	Proposed	**0.9621**	**0.9612**	**0.9673**	**0.9574**	**0.9253**
guggenheim	CV	0.9828	0.9826	0.9816	0.9838	0.9658
	FCMLSM	0.9841	0.9838	0.9834	0.9843	0.9682
	Chen	**0.9883**	**0.9882**	**0.9871**	**0.9895**	**0.9766**
	Proposed	0.9864	0.9862	0.9854	0.9872	0.9729
mountain	CV	0.9894	0.9807	0.9716	0.9905	0.9625
	FCMLSM	0.9901	0.9819	0.9730	0.9913	0.9646
	Chen	**0.9942**	**0.9893**	**0.9858**	0.9929	**0.9790**
	Proposed	0.9936	0.9883	0.9821	**0.9947**	0.9769

*The best segmentation performance is indicated in bold, and the second-best is underlined when applicable.

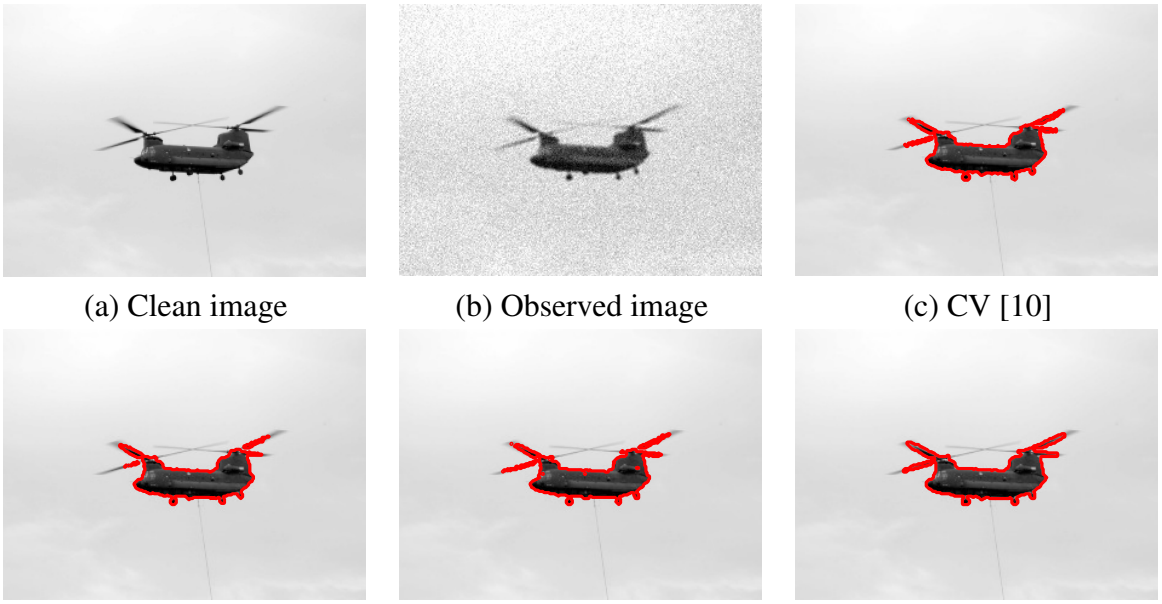

(a) Clean image (b) Observed image (c) CV [10]

(d) FCMLSM [53] (e) Chen [29] (f) Proposed

Figure 9. Segmentation results for a natural image corrupted by uniform blur and Rician noise. (a) Clean image, (b) observed image, and segmentation results obtained by (c) CV [10], (d) FCMLSM [53], (e) Chen [29], and (f) the proposed method.

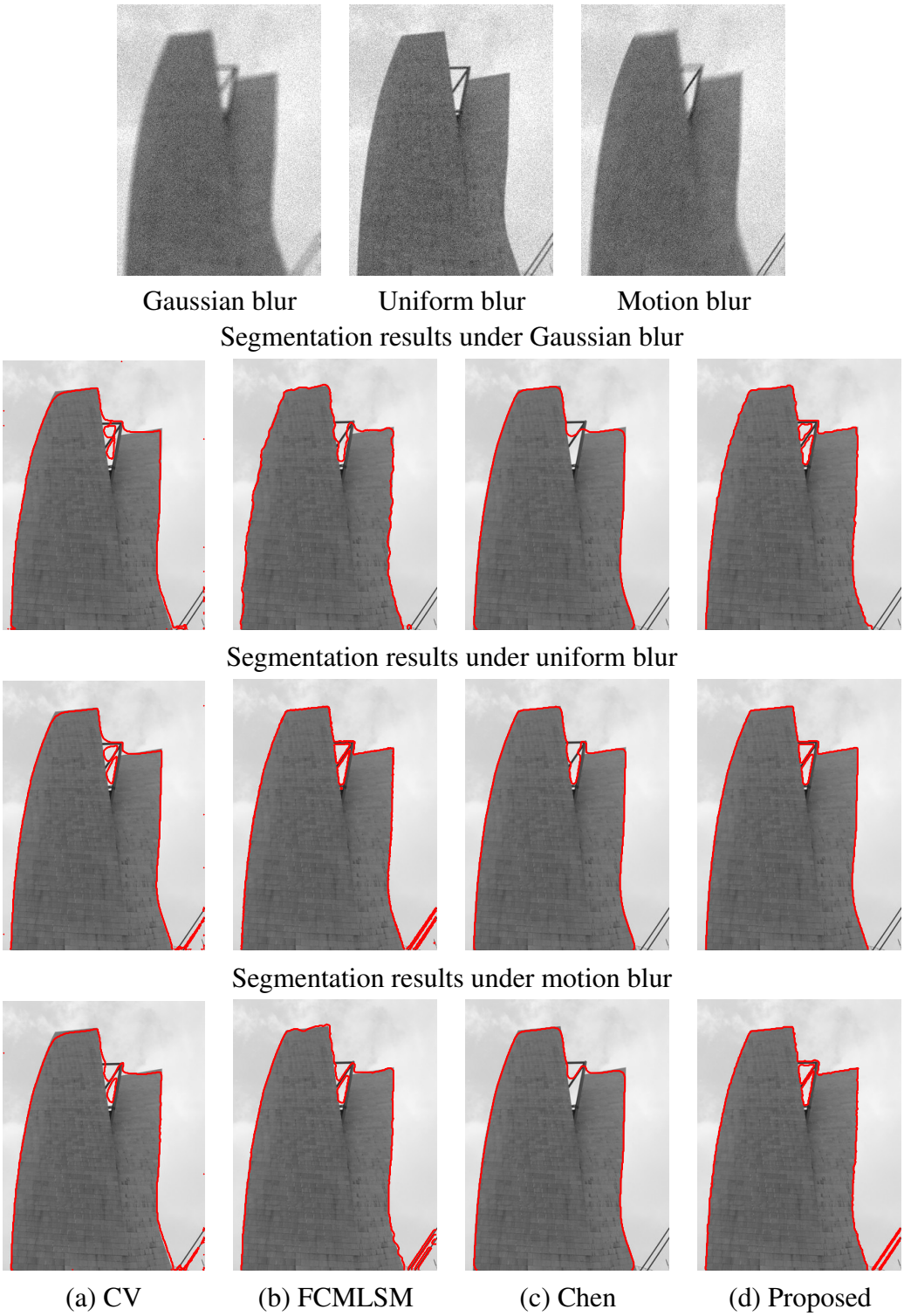

Figure 10. Segmentation results for a natural image corrupted by different blur kernels. Top row: observed images with Gaussian, uniform, and motion blur. Second to fourth rows: segmentation results corresponding to Gaussian blur, uniform blur, and motion blur, respectively. Columns correspond to segmentation results obtained by CV [10], FCMLSM [53], Chen [29], and the proposed method.

Figure 9 shows the segmentation results for all models under uniform blur, with corresponding zoomed-in views presented in Figure 11. Because the blur level is relatively mild, all models yield visually acceptable results. Nevertheless, the FCMLSM model incorrectly detects the left rotor of the helicopter, and the Chen model captures a small feature inside the helicopter. Among all methods, the proposed model yields the smoothest and most accurate helicopter boundary. These observations are consistent with the quantitative results reported in Table 2.

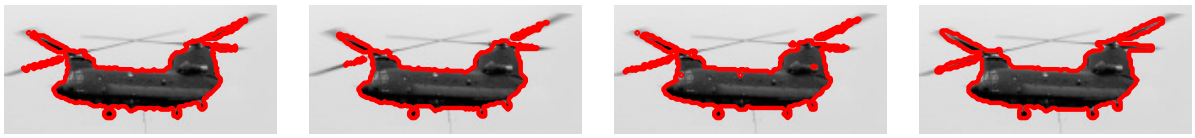

(a) CV [10] (b) FCMLSM [53] (c) Chen [29] (d) Proposed

Figure 11. Zoomed-in details of the segmentation results shown in Figure 9.

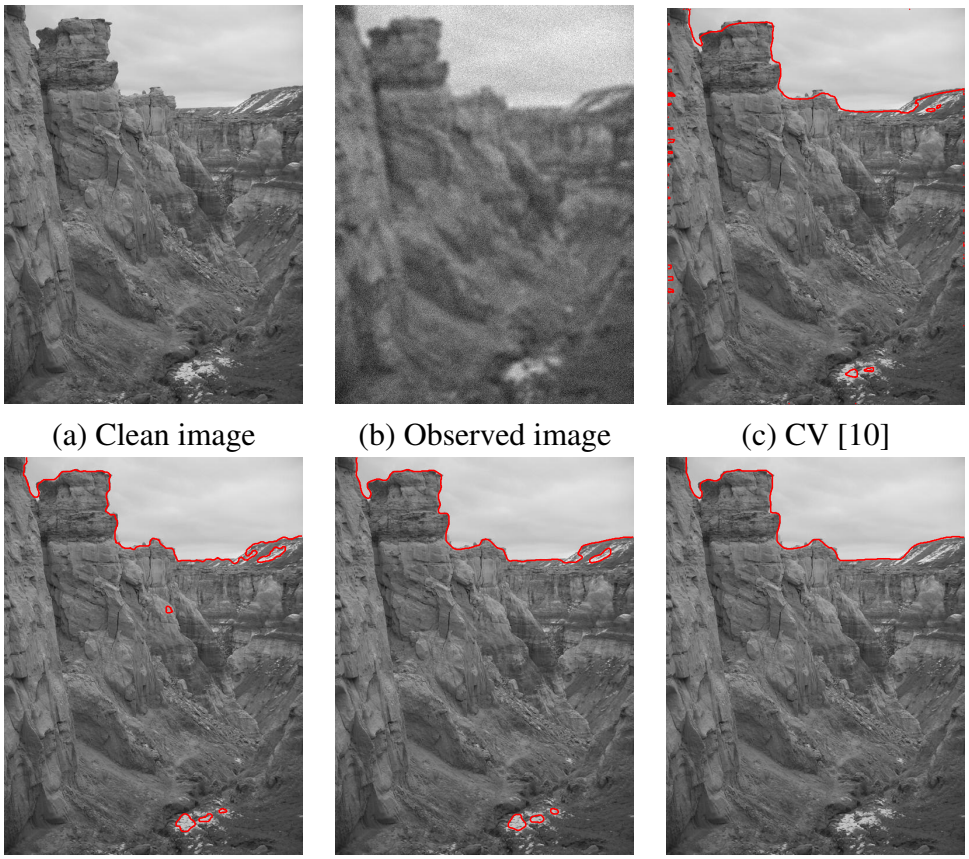

(a) Clean image (b) Observed image (c) CV [10]

(d) FCMLSM [53] (e) Chen [29] (f) Proposed

Figure 12. Segmentation results for a natural image corrupted by Gaussian blur and Rician noise. (a) Clean image, (b) observed image, and segmentation results obtained by (c) CV [10], (d) FCMLSM [53], (e) Chen [29], and (f) the proposed method.

Similar behavior is observed in Figure 12, where the CV model fails to accurately capture the mountain boundaries. Although the other models achieve relatively accurate segmentation, the

proposed model exhibits the least amount of false detections within the mountain region and provides more accurate boundaries.

In both the Chen method and our model, restoration is incorporated to assist the segmentation process. In Chen's approach, the restoration appears as an intermediate step, whereas in our model, it is performed jointly with the final segmentation. To illustrate this, the reconstructed images corresponding to the segmentation results in Figures 10 and 9 under uniform blur are shown in Figure 13.

These restored images differ from the original images: Fine details are smoothed while edges are enhanced, providing a piecewise-constant approximation suitable for segmentation. Consequently, peak signal-to-noise ratio (PSNR) and structural similarity index measure (SSIM) values are not necessarily high, as the objective is not conventional denoising but rather to facilitate piecewise-constant segmentation. In comparison, restoration by the Chen model often appears oversmoothed or slightly noisy, which can reduce segmentation effectiveness. The proposed method better preserves structural edges and produces restorations that more closely approximate piecewise-constant images. As a result, it achieves slightly higher PSNR and SSIM values and leads to more accurate and efficient segmentation.

As summarized in Tables 1–3, the proposed model achieves the highest accuracy, F-measure, precision, recall, and IoU values in most test cases. These results demonstrate the superiority of the proposed model over the other three methods in terms of segmentation performance.

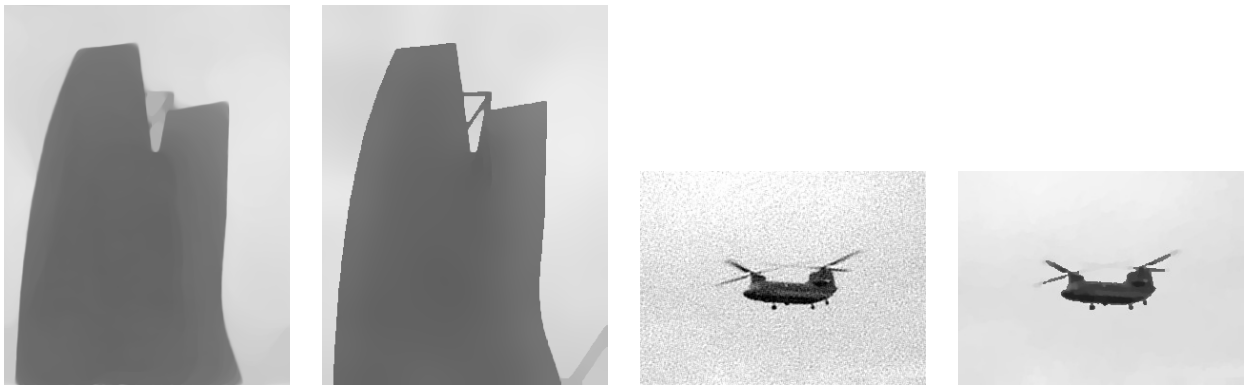

(a) Chen [29] (b) Proposed (c) Chen [29] (d) Proposed

Figure 13. Restoration results corresponding to Figures 10 and 9 under uniform blur. (a) and (b) show the restorations from Figure 10 using Chen [29] and the proposed method, respectively. (c) and (d) show the restorations from Figure 9 using Chen [29] and the proposed method, respectively. PSNR and SSIM values are (a) 26.59, 0.8521; (b) 29.02, 0.8581; (c) 25.51, 0.3363; (d) 29.68, 0.9601.

Numerical results are also presented to illustrate the convergence behavior of the proposed algorithm in practice. Figure 14 shows the evolution of the objective function value and the relative error curves of the variables u_i, g, and c_i with respect to the iteration number. The objective function decreases monotonically as the iterations proceed and stabilizes after a finite number of steps. Moreover, the relative errors exhibit a consistent and predictable decreasing trend. These observations are consistent with the theoretical convergence analysis and empirically indicate that the proposed

algorithm exhibits stable numerical behavior.

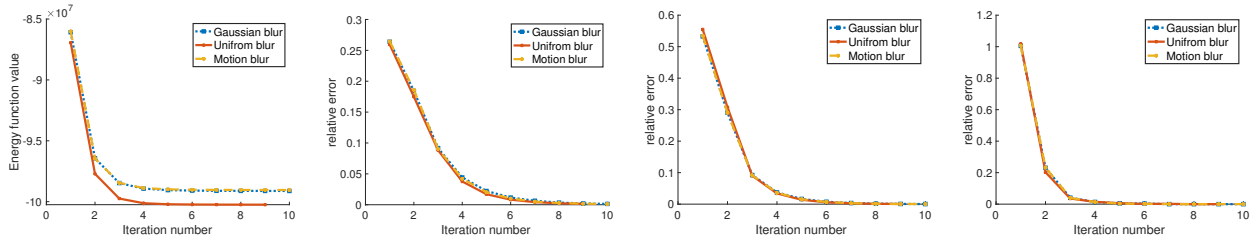

(a) energy function (b) relative error of g (c) relative error of c_i (d)relative error of u_i

Figure 14. Numerical convergence behavior of the proposed algorithm for Oscar image. The evolution of the objective function and the relative error curves of u, g, and c are shown with respect to the iteration number.

Figures 15–18 illustrate the segmentation results for MR images corrupted by Rician noise and blur, with Figure 17 showing the approximated images for Figures 15 and 16. All methods successfully capture the overall structure of thicker vessels. However, the CV and FCMLSM models are unable to accurately delineate vessel boundaries at the termini and are incapable of properly segmenting thin vessels. Both the Chen model and the proposed model achieve effective segmentation performance. For the Tubular image in Figure 15, the proposed model preserves the connectivity of the main vessel, whereas the Chen model segments it into multiple disconnected components.

In Figure 16, both models achieve similar connectivity, but the proposed model produces much more accurate vessel boundaries. In both cases, the proposed model provides smoother and more continuous boundaries while accurately capturing the geometry and branching structure of the vessels, as clearly seen in the approximated images in Figure 17. Furthermore, in Figure 18, the CV and FCMLSM models fail to correctly segment the interior dark gray region, whereas both the Chen model and the proposed model accurately identify interior features. With respect to the outer boundary, the proposed model provides significantly more accurate and consistent segmentation results. Overall, the proposed model demonstrates the most reliable performance, combining connectivity preservation, boundary smoothness, and accurate segmentation of thin vessels and interior features across all images.

Table 4. Average computing time (in seconds) of the proposed method and the comparison methods.

	Model			
Blur type	CV	FCMLSM	Chen	Proposed
Guassian blur	20.87	12.66	14.06	13.25
Uniform blur	18.84	10.63	10.87	12.75
Motion blur	18.20	14.78	14.67	14.48

In addition to the qualitative and quantitative comparisons, the computational efficiency of the proposed method is also evaluated. Table 4 reports the average computing time of the proposed method and the comparison methods. As shown in Table 4, all methods exhibit comparable computational costs, with average runtimes on the order of tens of seconds. The proposed method requires approximately 14 seconds on average, which is of the same order as the Chen and FCMLSM models, whereas the CV model exhibits a relatively higher computing time. Overall, the differences in

computational time are minor, indicating that the proposed method achieves improved segmentation and restoration performance without introducing additional computational overhead.

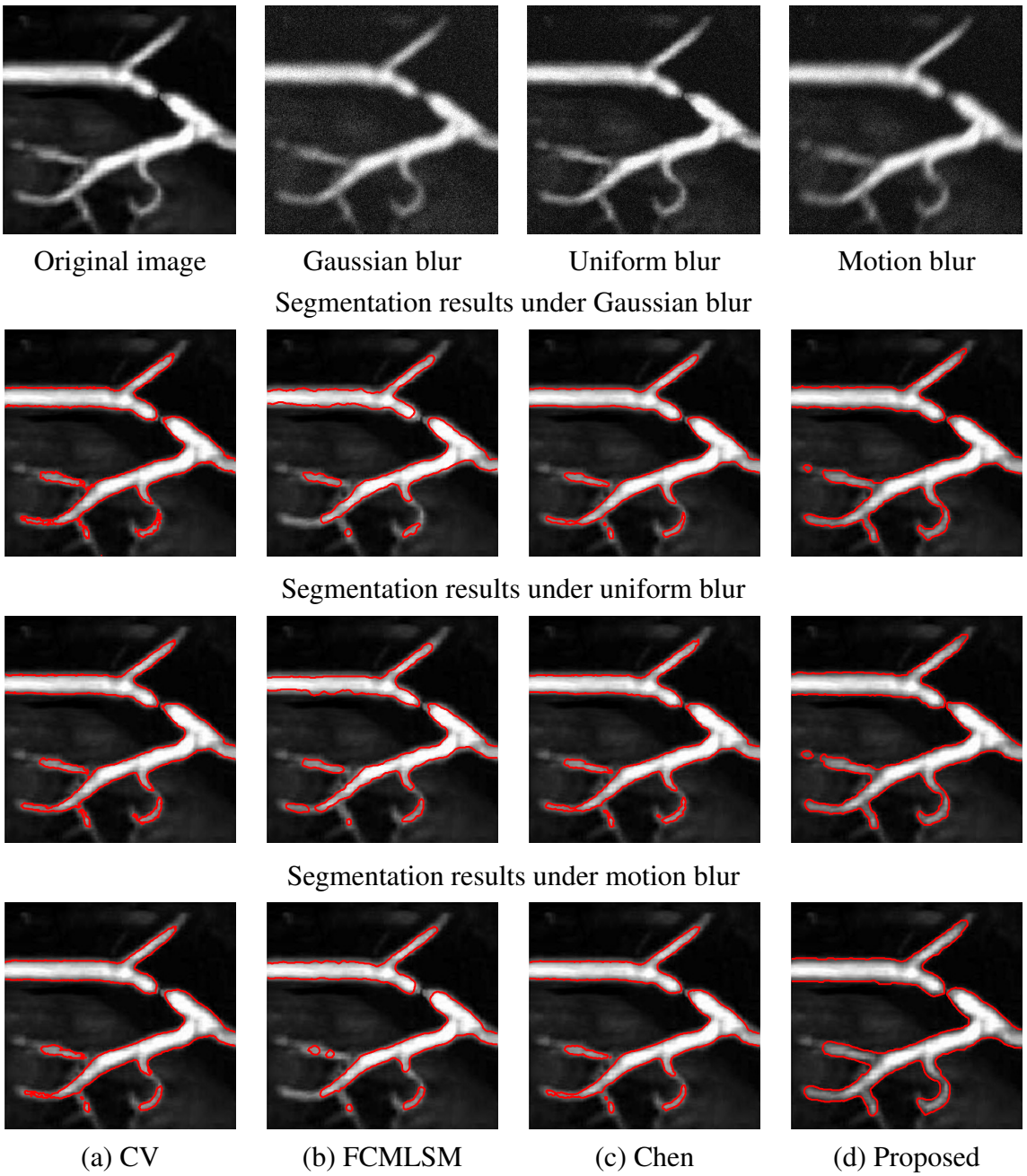

Figure 15. Segmentation results of an MR tubular image corrupted by Rician noise (σ = 5) under different blur kernels. The first row shows the original image and the observed images degraded by Gaussian, uniform, and motion blur, respectively. Rows 2–4 present the corresponding segmentation results under Gaussian blur, uniform blur, and motion blur, respectively. Columns correspond to the results obtained by different methods: CV [10], FCMLSM [53], Chen [29], and the proposed method.

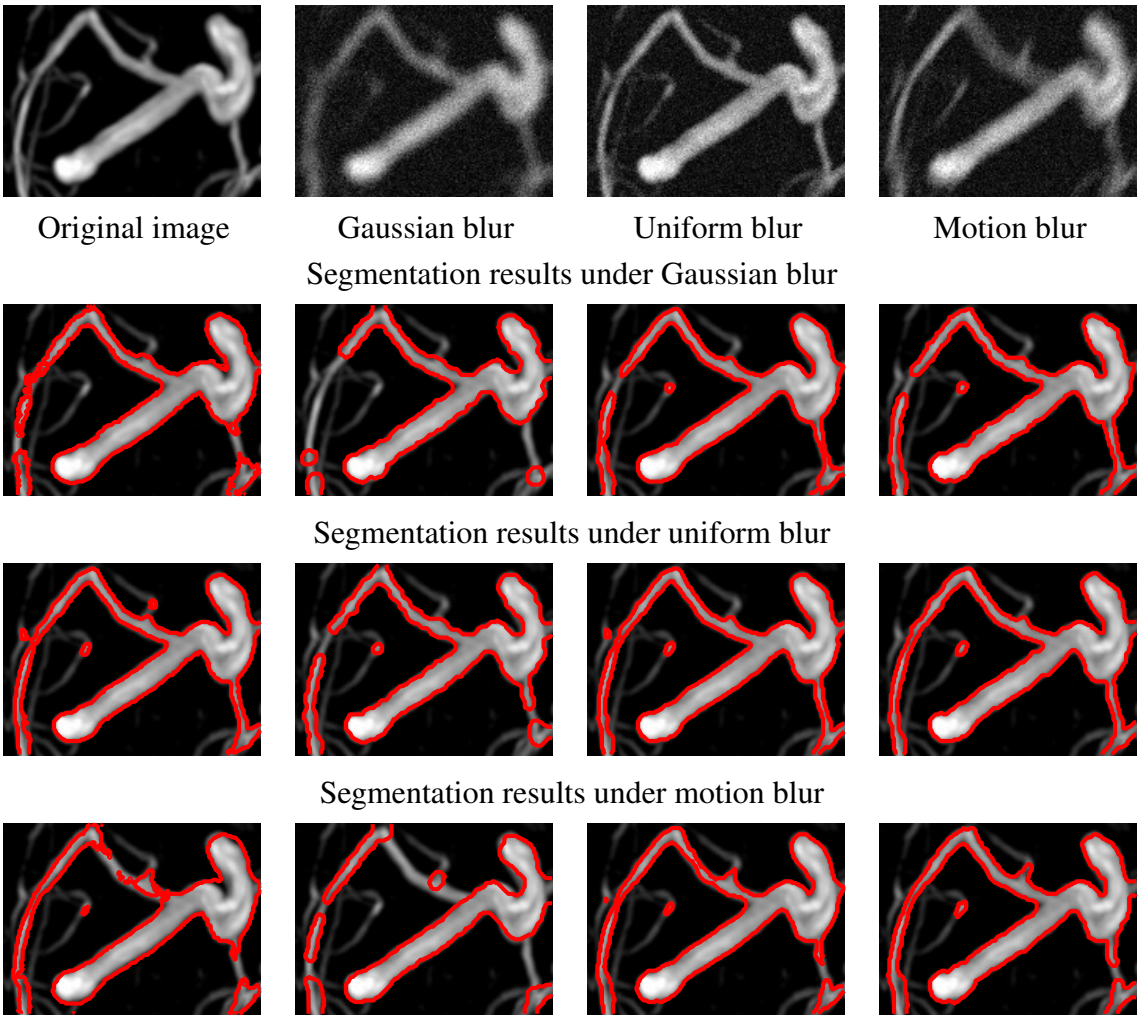

Figure 16. Segmentation results of an MR vessel image corrupted by Rician noise (σ = 5) under different blur kernels. The first row shows the original image and the observed images degraded by Gaussian, uniform, and motion blur, respectively. Rows 2–4 present the corresponding segmentation results under Gaussian blur, uniform blur, and motion blur, respectively. Columns correspond to the results obtained by different methods: CV [10], FCMLSM [53], Chen [29], and the proposed method.

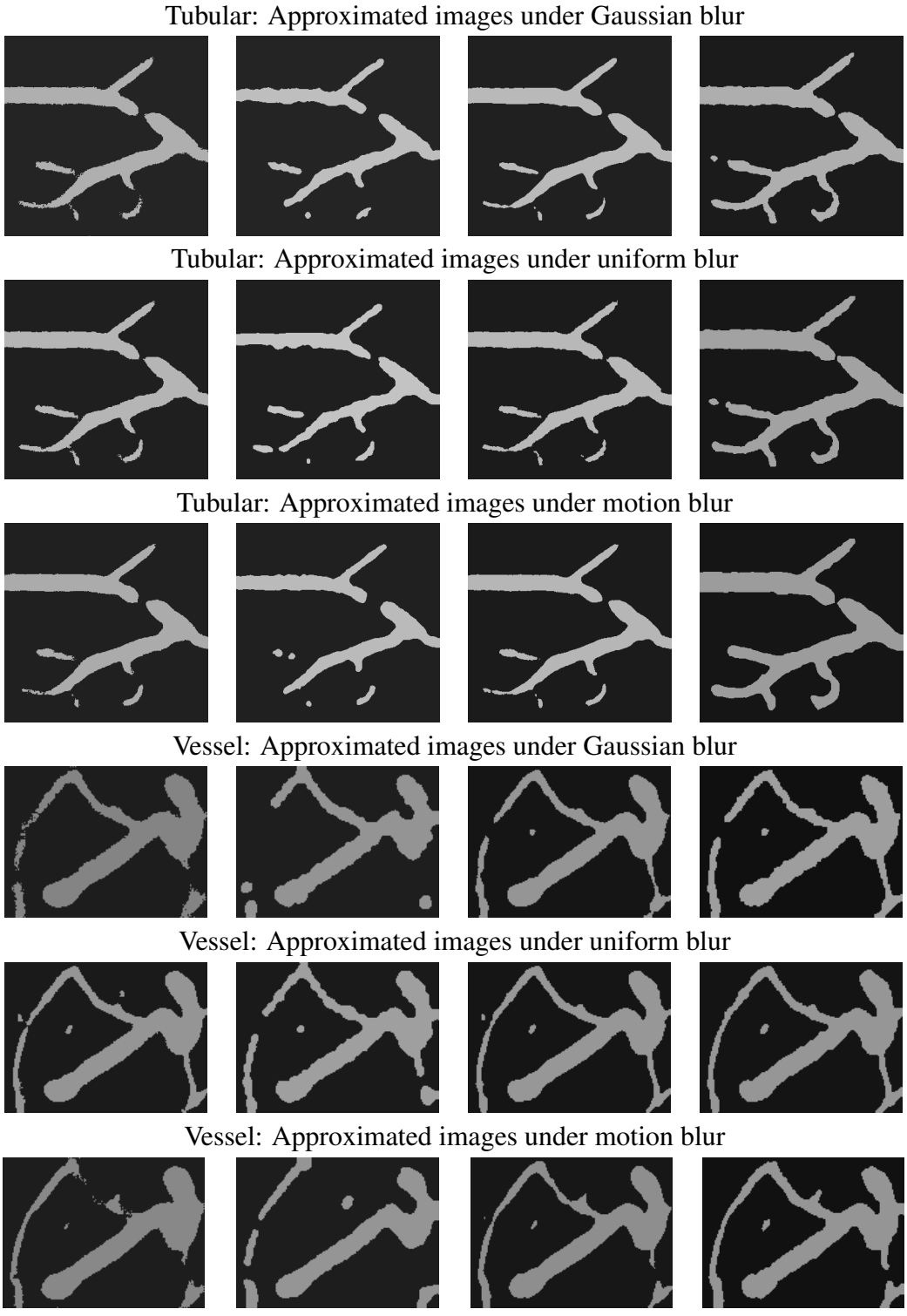

Figure 17. Approximated MR images under different blur types. Rows 1–3 correspond to Tubular1 (Gaussian, uniform, and motion blur), rows 4–6 correspond to Vessel3 (Gaussian, uniform, and motion blur). Columns show results obtained by CV [10], FCMLSM [53], Chen [29], and the proposed method.

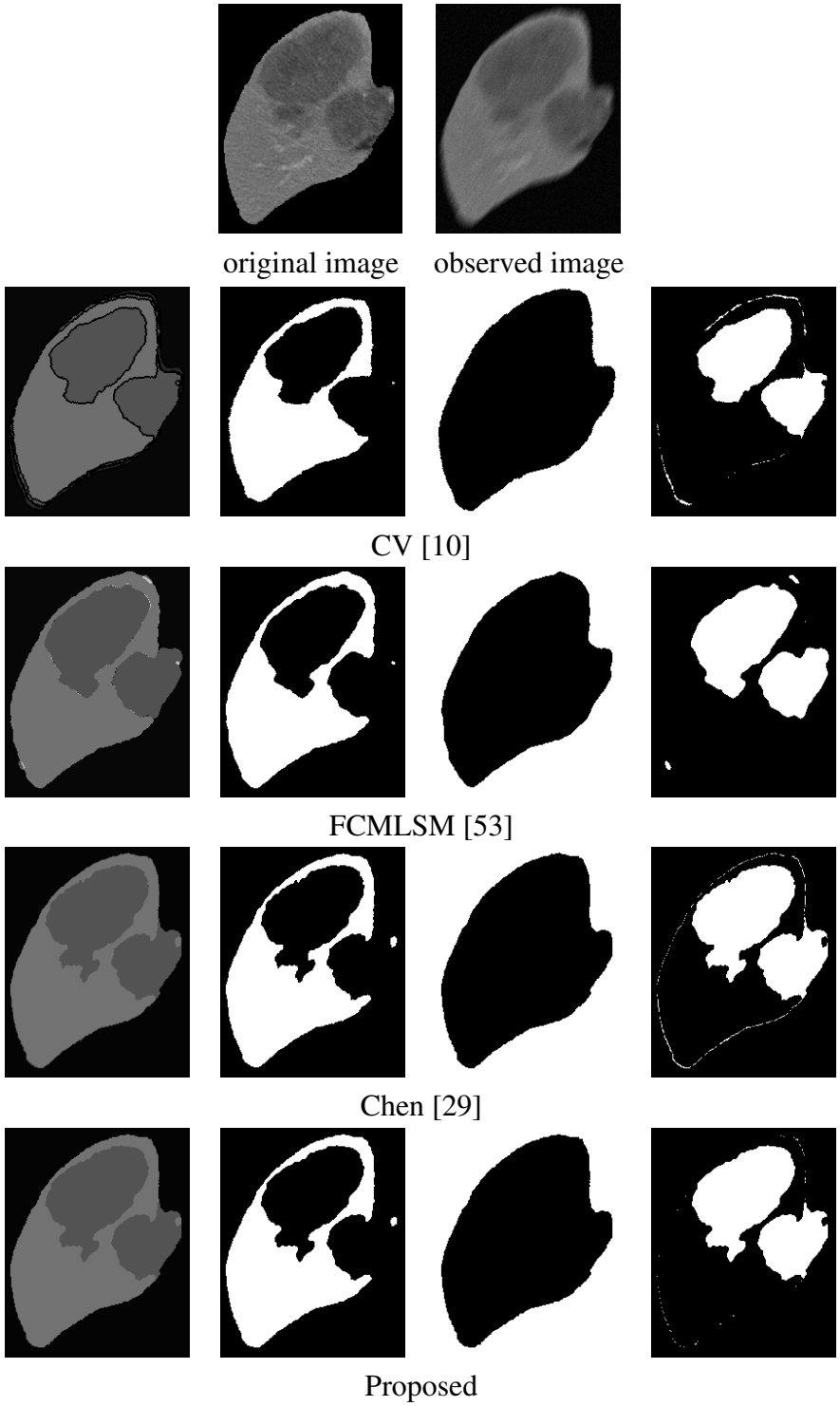

Figure 18. Multiphase segmentation results of a real liver tumor image. The first row shows the original image and the observed image corrupted by motion blur and noise. The second row shows the approximated images obtained by different methods. Rows 3–5 present the corresponding segmented phases. Columns correspond to the segmentation results obtained by different methods: CV [10], FCMLSM [53], Chen [29], and the proposed method.

6. Conclusions

In this article, the author proposed a coupled variational framework based on nonconvex total variation for image segmentation of images corrupted by Rician noise and blur. Within this framework, restoration and segmentation are jointly optimized, with restoration serving as an auxiliary component to enhance segmentation accuracy. The nonconvex total variation (NTV) regularization effectively suppresses noise while preserving important edge structures, resulting in clear and accurate segmentation. To solve the resulting nonconvex and nonsmooth optimization problem, a proximal alternating minimization algorithm was employed. An iteratively reweighted ℓ_1 algorithm was used to handle the nonconvex regularization terms, and the resulting subproblems were solved using the alternating direction method of multipliers. Numerical experiments demonstrate that the proposed method outperforms several state-of-the-art approaches in both visual quality and quantitative evaluation metrics. Future work will focus on extending the proposed framework to incorporate bias field correction for MR image segmentation.

Use of Generative-AI tools declaration

The author declares he has not used Artificial Intelligence (AI) tools in the creation of this article.

Acknowledgments

Myeongmin Kang was supported by Chungnam National University.

Conflict of interest

The author declares no conflicts of interest in this paper.

References

1. F. Li, M. K. Ng, T. Y. Zeng, C. Shen, A multiphase image segmentation method based on fuzzy region competition, *SIAM J. Imaging Sci.*, **3** (2010), 277–299. https://doi.org/10.1137/080736752
2. J. Zhang, J. Hu, Image segmentation based on 2D otsu method with histogram analysis, In: *2008 International conference on computer science and software engineering*, Wuhan, China, 2008, 105–108. https://doi.org/10.1109/CSSE.2008.206
3. S. Kim, M. Kang, Multiple-region segmentation without supervision by adaptive global maximum clustering, *IEEE Trans. Image Process.*, **21** (2011), 1600–1612. https://doi.org/10.1109/TIP.2011.2179058
4. W. Cai, S. Chen, D. Zhang, Fast and robust fuzzy c-means clustering algorithms incorporating local information for image segmentation, *Pattern Recogn.*, **40** (2007), 825–838. https://doi.org/10.1016/j.patcog.2006.07.011
5. M. Gong, Y. Liang, J. Shi, W. Ma, J. Ma, Fuzzy c-means clustering with local information and kernel metric for image segmentation, *IEEE Trans. Image Process.*, **22** (2013), 573–584. https://doi.org/10.1109/TIP.2012.2219547

6. J. Carreira, C. Sminchisescu, CPMC: Automatic object segmentation using constrained parametric min-cuts, *IEEE Trans. Pattern Anal.*, **34** (2012), 1312–1328. https://doi.org/10.1109/TPAMI.2011.231
7. J. Shi, J. Malik, Normalized cuts and image segmentation, *IEEE Trans. Pattern Anal.*, **22** (2000), 888–905. https://doi.org/10.1109/34.868688
8. P. F. Felzenszwalb, D. P. Huttenlocher, Efficient graph-based image segmentation, *Int. J. Comput. Vision*, **59** (2004), 167–181. https://doi.org/10.1023/B:VISI.0000022288.19776.77
9. D. Mumford, J. Shah, Optimal approximations by piecewise smooth functions and associated variational problems, *Commun. Pure Appl. Math.*, **42** (1989), 577–685. https://doi.org/10.1002/cpa.3160420503
10. T. Chan, L. Vese, An active contour model without edges, In: *Scale-space theories in computer vision*, Berlin, Heidelberg: Springer, 1999, 141–151. https://doi.org/10.1007/3-540-48236-9_13
11. S.-H. Lee, J. K. Seo, Level set-based bimodal segmentation with stationary global minimum, *IEEE Trans. Image Process.*, **15** (2006), 2843–2852. https://doi.org/10.1109/TIP.2006.877308
12. X. Cai, R. Chan, T. Zeng, A two-stage image segmentation method using a convex variant of the Mumford–Shah model and thresholding, *SIAM J. Imaging Sci.*, **6** (2013), 368–390. https://doi.org/10.1137/120867068
13. L. Bar, N. Sochen, N. Kiryati, Variational pairing of image segmentation and blind restoration, In: *Computer Vision - ECCV 2004*, Berlin, Heidelberg: Springer, 2004, 166–177. https://doi.org/10.1007/978-3-540-24671-8_13
14. X. Cai, Variational image segmentation model coupled with image restoration achievements, *Pattern Recogn.*, **48** (2015), 2029–2042. https://doi.org/10.1016/j.patcog.2015.01.008
15. G. Gerig, O. Kubler, R. Kikinis, F. A. Jolesz, Nonlinear anisotropic filtering of MRI data, *IEEE Trans. Med. Imaging*, **11** (1992), 221–232. https://doi.org/10.1109/42.141646
16. K. Krissian, S. Aja-Fernández, Noise-driven anisotropic diffusion filtering of MRI, *IEEE Trans. Image Process.*, **18** (2009), 2265–2274. https://doi.org/10.1109/TIP.2009.2025553
17. C. S. Anand, J. S. Sahambi, Wavelet domain non-linear filtering for MRI denoising, *Magn. Reson. Imaging*, **28** (2010), 842–861. https://doi.org/10.1016/j.mri.2010.03.013
18. R. D. Nowak, Wavelet-based Rician noise removal for magnetic resonance imaging, *IEEE Trans. Image Process.*, **8** (1999), 1408–1419. https://doi.org/10.1109/83.791966
19. D. W. Kim, C. Kim, D. H. Kim, D. H. Lim, Rician nonlocal means denoising for MRI images using nonparametric principal component analysis, *EURASIP J. Image Vide.*, **2011** (2011), 15. https://doi.org/10.1186/1687-5281-2011-15
20. J. Yang, J. Fan, D. Ai, S. Zhou, S. Tang, Y. Wang, Brain MR image denoising for rician noise using pre-smooth non-local means filter, *Biomed. Eng. Online*, **14** (2015), 1–20. http://doi.org/10.1186/1475-925X-14-2
21. S. Basu, T. Fletcher, R. Whitaker, Rician noise removal in diffusion tensor MRI, In: *Medical image computing and computer-assisted intervention–MICCAI 2006*, 2006, Berlin, Heidelberg: Springer, 117–125. https://doi.org/10.1007/11866565_15

22. P. Getreuer, M. Tong, L. A. Vese, A variational model for the restoration of MRI images corrupted by blur and Rician noise, In: *Advances in visual computing. ISVC 2011*, 2011, Berlin, Heidelberg: Springer, 686–698. https://doi.org/10.1007/978-3-642-24028-7_63

23. L. Chen, T. Zeng, A convex variational model for restoring blurred images with large Rician noise, *J. Math. Imaging Vis.*, **53** (2015), 92–111. https://doi.org/10.1007/s10851-014-0551-y

24. A. Martín, E. Schiavi, S. S. de León, On 1-Laplacian elliptic equations modeling magnetic resonance image Rician denoising, *J. Math. Imaging Vis.*, **57** (2017), 202–224. https://doi.org/10.1007/s10851-016-0675-3

25. T. D. K. Phan, A spatially variant high-order variational model for Rician noise removal, *PeerJ Comput. Sci.*, **9** (2023), e1579. https://doi.org/10.7717/peerj-cs.1579

26. K. Brzostowski, R. Obuchowicz, Combining variational mode decomposition with regularisation techniques to denoise MRI data, *Magn. Reson. Imaging*, **106** (2024), 55–76. https://doi.org/10.1016/j.mri.2023.10.011

27. D. Wei, S. Weng, F. Li, Nonconvex Rician noise removal via convergent plug-and-play framework, *Appl. Math. Model.*, **123** (2023), 197–212. https://doi.org/10.1016/j.apm.2023.06.033

28. X. Wu, S. Bricq, C. Collet, Brain MRI segmentation and lesion detection using generalized gaussian and Rician modeling, In: *Proceedings volume 7962, medical imaging 2011: image processing*, Lake Buena Vista (Orlando), Florida, United States, 2011, 796236. https://doi.org/10.1117/12.871384

29. L. Chen, Y. Li, T. Zeng, Variational image restoration and segmentation with Rician noise, *J. Sci. Comput.*, **78** (2019), 1329–1352. https://doi.org/10.1007/s10915-018-0826-3

30. D. Jiang, W. Dou, L. Vosters, X. Xu, Y. Sun, T. Tan, Denoising of 3D MRI images with multi-channel residual learning of convolutional neural network, *Jpn. J. Radiol.*, **36** (2018), 566–574. https://doi.org/10.1007/s11604-018-0758-8

31. S. Li, J. Zhou, D. Liang, Q. Liu, MRI denoising using progressively distribution-based neural network, *Magn. Reson. Imaging*, **71** (2020), 55–68. https://doi.org/10.1016/j.mri.2020.04.006

32. X. You, N. Cao, H. Lu, M. Mao, W. Wang, Denoising of MRI images with Rician noise using a wider neural network and noise range division, *Magn. Reson. Imaging*, **64** (2019), 154–159. https://doi.org/10.1016/j.mri.2019.05.042

33. C.-C. Wu, C.-H. Hsu, P. C. Wang, T.-W. Tu, Y.-Y. Hsu, Influence of Rician noise on cardiac MR image segmentation using deep learning, In: *Intelligent systems design and applications. ISDA 2023*, Cham: Springer, 2023, 223–232. https://doi.org/10.1007/978-3-031-64813-7_24

34. L. I. Rudin, S. Osher, E. Fatemi, Nonlinear total variation based noise removal algorithms, *Physica D*, **60** (1992), 259–268. https://doi.org/10.1016/0167-2789(92)90242-F

35. D. Geman, C. Yang, Nonlinear image recovery with half-quadratic regularization, *IEEE Trans. Image Process.*, **4** (1995), 932–946. https://doi.org/10.1109/83.392335

36. M. C. Robini, A. Lachal, I. E. Magnin, A stochastic continuation approach to piecewise constant reconstruction, *IEEE Trans. Image Process.*, **16** (2007), 2576–2589. https://doi.org/10.1109/TIP.2007.904955

37. D. Krishnan, R. Fergus, Fast image deconvolution using hyper-Laplacian priors, In: *Advances in neural information processing systems 22 (NIPS 2009)*, 2009, 1033–1041.

38. M. Nikolova, M. K. Ng, C.-P. Tam, Fast nonconvex nonsmooth minimization methods for image restoration and reconstruction, *IEEE Trans. Image Process.*, **19** (2010), 3073–3088. https://doi.org/10.1109/TIP.2010.2052275

39. H. Attouch, J. Bolte, P. Redont, A. Soubeyran, Proximal alternating minimization and projection methods for nonconvex problems: An approach based on the Kurdyka-Łojasiewicz inequality, *Math. Oper. Res.*, **35** (2010), 438–457. https://doi.org/10.1287/moor.1100.0449

40. H. Attouch, J. Bolte, B. F. Svaiter, Convergence of descent methods for semi-algebraic and tame problems: proximal algorithms, forward–backward splitting, and regularized gauss–seidel methods, *Math. Program.*, **137** (2013), 91–129. https://doi.org/10.1007/s10107-011-0484-9

41. P. Ochs, A. Dosovitskiy, T. Brox, T. Pock, On iteratively reweighted algorithms for nonsmooth nonconvex optimization in computer vision, *SIAM J. Imaging Sci.*, **8** (2015), 331–372. https://doi.org/10.1137/140971518

42. T. Sun, P. Yin, L. Cheng, H. Jiang, Alternating direction method of multipliers with difference of convex functions, *Adv. Comput. Math.*, **44** (2018), 723–744. https://doi.org/10.1007/s10444-017-9559-3

43. T. Sun, H. Jiang, L. Cheng, W. Zhu, Iteratively linearized reweighted alternating direction method of multipliers for a class of nonconvex problems, *IEEE Trans. Signal Process.*, **66** (2018), 5380–5391. https://doi.org/10.1109/TSP.2018.2868269

44. T. Sun, R. Barrio, M. Rodríguez, H. Jiang, Inertial nonconvex alternating minimizations for image deblurring, *IEEE Trans. Image Process.*, **28** (2019), 6211–6224. https://doi.org/10.1109/TIP.2019.2917980

45. L. A. Vese, T. F. Chan, A multiphase level set framework for image segmentation using the Mumford and Shah model, *Int. J. Comput. Vis.*, **50** (2002), 271–293. https://doi.org/10.1023/A:1020874308076

46. Y. Yang, B. Wu, A new and fast multiphase image segmentation model for color images, *Math. Probl. Eng.*, **2012** (2012), 494761, 494761. https://doi.org/10.1155/2012/494761

47. Y. He, M. Y. Hussaini, J. Ma, B. Shafei, G. Steidl, A new fuzzy c-means method with total variation regularization for segmentation of images with noisy and incomplete data, *Pattern Recogn.*, **45** (2012), 3463–3471. https://doi.org/10.1016/j.patcog.2012.03.009

48. R. Chan, H. Yang, T. Zeng, A two-stage image segmentation method for blurry images with poisson or multiplicative gamma noise, *SIAM J. Imaging Sci.*, **7** (2014), 98–127. https://doi.org/10.1137/130920241

49. T. Goldstein, S. Osher, The split Bregman method for l1-regularized problems, *SIAM J. Imaging Sci.*, **2** (2009), 323–343. https://doi.org/10.1137/080725891

50. S. Boyd, N. Parikh, E. Chu, B. Peleato, J. Eckstein, Distributed optimization and statistical learning via the alternating direction method of multipliers, *Found. Trends Mach. Learn.*, **3** (2011), 1–122. https://doi.org/10.1561/2200000016

51. A. Chambolle, T. Pock, A first-order primal-dual algorithm for convex problems with applications to imaging, *J. Math. Imaging Vis.*, **40** (2011), 120–145. https://doi.org/10.1007/s10851-010-0251-1

52. Y. Chen, X. Ye, Projection onto a simplex, arXiv:1101.6081.

53. B. N. Li, C. K. Chui, S. Chang, S. H. Ong, Integrating spatial fuzzy clustering with level set methods for automated medical image segmentation, *Comput. Biol. Med.*, **41** (2011), 1–10. https://doi.org/10.1016/j.compbiomed.2010.10.007

54. S. Alpert, M. Galun, A. Brandt, R. Basri, Image segmentation by probabilistic bottom-up aggregation and cue integration, *IEEE Trans. Pattern Anal.*, **34** (2012), 315–327. https://doi.org/10.1109/TPAMI.2011.130

55. P. Bideau, A. RoyChowdhury, R. R. Menon, E. Learned-Miller, The best of both worlds: combining CNNs and geometric constraints for hierarchical motion segmentation, In: *2018 IEEE/CVF Conference on computer vision and pattern recognition*, Salt Lake City, UT, USA 2018, 508–517. https://doi.org/10.1109/CVPR.2018.00060

56. K.-S. Chuang, H.-L. Tzeng, S. Chen, J. Wu, T.-J. Chen, Fuzzy C-means clustering with spatial information for image segmentation, *Comput. Med. Imag. Grap.*, **30** (2006), 9–15. https://doi.org/10.1016/j.compmedimag.2005.10.001

57. P. Getreuer, Total variation deconvolution using split Bregman, *Image Process. On Line*, **2** (2012), 158–174. https://doi.org/10.5201/ipol.2012.g-tvdc

AIMS Press

© 2026 the Author(s), licensee AIMS Press. This is an open access article distributed under the terms of the Creative Commons Attribution License (https://creativecommons.org/licenses/by/4.0)